Clinico-genomic features predict distinct metastatic phenotypes in cutaneous melanoma

Tyler J. Aprati[1,2,3], Chi-Ping Day[4], Daniel Lee[5], Alexander Pan[5], Justin Jee[6], Giuseppe Tarantino[1,2,3], Michael P. Manos[1], Hannah Faulkner[1], Marta M. Holovatska[1], Karam Khaddour[1,3], Catherine H. Feng[1], Kelly P. Burke[1,2,3,14], Marc Glettig[1,2,9], Zoe Weaver Ohler[8], Rajaa El Meskini[8], F. Stephen Hodi[1,3], Rizwan Haq[1,3], Alexander N. Shoushtari[6,10], Nikolaus Schultz[6], Jeffrey J. Ishizuka[5,11,12,13], Alexander Gusev[1,2,3], Maryclare Griffith[7], Kenneth L. Kehl[1,3], and David Liu[1,2,3,*]

[1]Department of Medical Oncology, Dana-Farber Cancer Institute, Boston, MA, USA, [2]Broad Institute of MIT and Harvard, Cambridge, MA, USA, [3]Harvard Medical School, Boston, MA, USA, [4]Cancer Data Science Laboratory, Center for Cancer Research, National Cancer Institute, NIH, MD, USA, [5]Yale Cancer Center, CT, USA, [6]Memorial Sloan Kettering Cancer Center, NY, USA, [7]University of Massachusetts Amherst, MA, USA, [8]Center for Advanced Preclinical Research, Frederick National Laboratory for Cancer Research, National Cancer Institute, Frederick, MD, USA, [9]ETH Zürich, Zürich, Switzerland, [10]Weill Cornell Medical College, [11]Department of Internal Medicine (Oncology), Yale School of Medicine, New Haven, CT, USA, [12]Department of Immunobiology, Yale School of Medicine, New Haven, CT, USA, [13]Department of Pathology, Yale School of Medicine, New Haven, CT, USA, [14]Department of Immunology, Blavatnik Institute, Harvard Medical School, MA, USA

[*]Corresponding author: David Liu, david_liu@dfci.harvard.edu

Abstract

Metastasis drives mortality and morbidity in cancer. While some patients develop broad metastatic disease across multiple organs, others exhibit organ-specific spread. To identify mechanisms underlying metastatic organotropism, we analyzed clinico-genomic data from over 7,000 patients with metastatic cutaneous melanoma in three independent cohorts (one primary discovery and two validation cohorts including a nationwide electronic health record-derived deidentified database), leveraging machine learning approaches to clinical data. We found that female sex and increased tumor mutational burden associate with decreased metastatic potential, while older age associates with more lung and adrenal metastases. Using unsupervised analyses, patients clustered into five metastatic patterns: a “highly metastatic” cluster characterized by involvement of many organs, a “low metastatic” cluster characterized by few metastatic sites (mostly lymph node metastases), and three additional clusters each characterized by metastasis to specific sites (brain, lung, liver). Mutations in *B2M* and *PTEN* associated with increased overall metastatic potential. *PTEN* mutations were also associated with brain metastases but were enriched only in the “highly metastatic” cluster and not the brain-specific cluster. Mutations in *GNAQ* or *GNA11 (GNA)* associated with increased liver metastasis. To validate this association, we tested and demonstrated liver tropism in two GNA-mutant genetically engineered cutaneous melanoma mouse models of metastasis. Overall, our study elucidates distinct phenotypes of metastasis in patients with melanoma and identifies novel clinical and genomic associations that illuminate the clinical drivers of metastatic organotropism.

Introduction

Metastasis is a hallmark of cancer and the primary driver of cancer mortality and morbidity in solid tumors[1]. The "seed-soil" hypothesis posits that interactions between tumor-intrinsic features and organ-specific microenvironmental factors enable metastases to form[2]. The propensity of a cancer to metastasize to specific organs, a process known as metastatic organotropism, differs by tumor histology[3]. While some cancers tend to metastasize to specific sites (prostate cancer to the bone, colorectal cancer to the liver and lung), others (melanoma, non-small cell lung cancer, clear cell renal carcinoma) display large heterogeneity between patients, with the capacity to metastasize to virtually any organ[4]. To this end, preclinical studies have unraveled mechanisms of metastasis[1,5] and nominated mechanisms of site-specific metastasis in certain settings[6,7], yet the clinical patterns and drivers of metastasis in patients are less well-understood, despite clear data that site-specific metastases have prognostic and predictive significance[8,9]. Recently, clinico-genomic datasets with metastatic annotations have been generated in five cancer types[10] or pan-cancer[11] utilizing different methods for annotation of metastatic sites (i.e. machine learning methods on electronic health record data[12,13,10] or ICD9 codes). These studies identified some genomic markers associated with overall metastatic potential across tumor histologies (e.g. fraction of genome altered[11]) and novel markers associated with better response to immunotherapy in a specific histology (*SETD2* mutations associated with improved survival on immunotherapy in NSCLC[10]). Another recent study explored metastasis specifically in lung adenocarcinoma[14], finding that male sex and younger age was associated with development of metastasis, and that *TP53* mutations and patterns of APOBEC mutagenesis were associated with metastatic incidence and burden. Despite these recent advances and past work in autopsy studies[15–18], little is understood about the patient-to-patient differences in patterns of metastasis and temporal patters of metastases, which is critical to elucidating (and eventually targeting) the different biological mechanisms driving metastasis in patients.

To address these issues, we perform a deep analysis of metastasis patterns and their genomic and clinical correlates in over 7000 cutaneous melanoma patients from 3 independent cohorts (one primary discovery, two as validation cohorts) with different methods of longitudinal metastatic site abstraction and genomic sequencing. Cutaneous melanoma has broad and clinically heterogeneous metastasis patterns and well-characterized and clinically relevant genomic drivers, making it particularly well-suited for the analysis.

We identify major patterns of metastasis in patients, specifically subgroups with high and low-metastatic potential and subgroups dominated by specific metastatic sites (brain, lung, and liver). We validate these patterns in an orthogonal patient population. Using time-to-event models, we identify clinical and genomic correlates of metastasis and site-specific organotropism. Overall, female sex and higher tumor mutational burden (TMB) associated with decreased metastatic potential, while older age associated with lung and adrenal-specific metastasis. Two alterations previously demonstrated to be associated with immunotherapy resistance, loss-of-function mutations in *B2M* and *PTEN,* were identified as the strongest predictors of broad metastasis. As previously observed, *PTEN* mutations were associated with brain metastases in our cohort, but specifically as part of a broad program of metastasis; it was not enriched among patients with specific metastatic tropism to the brain. Indeed,

brain metastases in the highly metastatic cluster of patients had distinct clinical and genomic features from the brain metastases in the cluster of brain-tropic metastatic patients. Lastly, hot-spot mutations in *GNAQ* and *GNA11* strongly associated with rapid acquisition of liver metastasis, which validated in an independent patient cohort, and we found supporting functional evidence in preclinical mouse models. Overall, our approach in this study provides a comprehensive analysis of metastasis in cutaneous melanoma and a framework for exploration of organotropism that can be applied to other tumor types.

Results

Clinical and genomic characteristics of discovery cohort

We identified 881 patients with available next-generation sequencing[19] (NGS) of their melanoma tumors from 2005 to 2023 at Dana-Farber Cancer Institute (DFCI). We collected 26,117 text imaging reports from these patients, utilizing a natural language processing (NLP) model to annotate presence of cancer and presence of metastatic sites[12,13]. After filtering for patients with metastatic cutaneous melanoma and imaging scans relevant for metastatic site annotations (Methods), our final cohort consisted of 13,033 cancer relevant scans across 455 patients (Fig. 1a-b). Patients with cutaneous melanoma had a median follow up of 19 months and a median of 22 annotated reports. The median age of patients was 64 years old at time of first radiographic evidence of cancer, and 64% of the patients were male. Annotated sites of metastasis included brain, bone, lymph node (LN), lung, liver, adrenal gland, and peritoneum (Fig. 1c). For each patient, we generated time to each site-specific metastasis, utilizing the first radiographic report with cancer detected as reference time zero.

We next analyzed the 472 NGS panel sequenced tumors from these patients. 17 patients had more than one available sequenced biopsy, and information was aggregated for these patients (Fig. 1b) (Methods). Tumor tissue used for sequencing was primarily from metastatic (vs primary) sites and most often from skin biopsies (Supp Fig. 1a-b). Mutations in 158 genes common to all versions of the targeted panel sequencing were included and filtered for functionally relevant alterations (Methods). 41% had mutations in BRAF, 33% in NRAS, and 20% in NF1 (Supp Fig. 1c), consistent with previously reported driver mutation frequencies[20]. TMB values for the cohort had a mean of 21.2 Mt/Mb and a standard deviation of 19.5 Mt/Mb. Further cohort details can be found in Supplementary Tables.

Patients had an average of 2.97 organs of metastasis (median 3, mode 2) in the follow-up period (Fig. 1d). Lung and lymph node were the most common metastatic sites (~ 70% lifetime), followed by bone, brain, and liver metastatic sites (35-45%), and peritoneal and adrenal metastatic sites (~ 20% lifetime) (Fig. 1e). The most common combinations of metastatic sites across patient lifetime were lung and LN, lung only, and brain only, which occurred in 9%, 7%, and 4% of patients, respectively (Supp Fig. 1d). We visualized metastasis longitudinally using a swimmer plot (Fig. 1f). At 4 years after first radiographic evidence of cancer, we observed a cumulative metastatic incidence of 66% (lymph node), 60% (lung), 39% (bone), 35% (brain), 30% (liver), 19% (peritoneal), and 16% (adrenal) (Fig. 1g). The acquisition of metastatic sites was concordant with their lifetime frequency: lymph node and lung metastases were frequent and occurred earlier; bone, brain, and liver metastases were less frequent and occurred throughout patient follow-up; adrenal and peritoneal metastases were rare

and occurred later in the disease progression.

Association of site-specific metastasis on survival and other metastasis

We then evaluated how development of site-specific metastasis predicts overall survival and later metastasis, modeling site-specific metastases as time-dependent covariates and adjusting for total number of other metastatic sites (Fig. 2a).

Not surprisingly, development of any metastatic site was associated with worse survival, but liver and brain metastases had the worst effects on survival (HR[95% CI] = 2.77[2.02-3.82], 2.18[1.58-3.0], respectively, all $p < 0.001$). The associations between sites and survival and ordering of effects appear consistent with previous exploration of survival differences by first detected site of metastasis[21].

We next tested whether the prognostic impact on survival of developing a metastatic site was dependent on the number of other metastatic sites, e.g. if the effect on overall survival differs if a metastatic site is, for instance, the first or fifth site of disease (Fig. 2b). Interestingly, liver and brain metastases were different; brain metastasis conferred a 589% increased rate of death as the first site of metastasis, while as the fifth site of metastasis only conferred a 47% increased rate of death (Brain HR = 6.89, 95% CI [3.63-13.09], $p < 0.001$; number of met sites:brain interaction HR = 0.68, 95% CI [0.56-0.82], $p < 0.001$). On the other hand, liver metastasis conferred an estimated 192% increased rate of death without statistically significant evidence of interaction with the number of other metastatic sites (Liver HR = 2.92, 95% CI [1.54-5.55], $p = 0.001$; number of met sites:liver interaction HR = 0.98, 95% CI [0.81-1.19], $p = 0.86$).

We then examined the associations between site-specific metastasis and overall lifetime metastatic burden. Adrenal and peritoneal metastases were associated with the highest metastatic burden, lung and lymph node metastases were associated with the lowest overall metastatic burden, and liver, bone, and brain metastases were associated with intermediate metastatic burden (Fig. 2c, Supp Fig. 1e).

We next investigated associations between metastatic sites. In a lifetime analysis, the presence of a metastatic site was associated with the presence of a metastasis to a second site across all site-site combinations, adjusting for the total number of metastatic sites (Supp Fig. 1f) (Methods). We then took a temporal approach, modeling the time-dependent relationship between a specific site of metastasis and subsequent development of another site of metastasis, adjusting for the total number of metastatic sites (Fig 2d, Methods). The strongest associations observed were increased rates of developing brain or lymph node metastases in patients after development of peritoneal metastases (HR = 2.15, 95% CI [1.24-3.73], $p = 0.006$; HR = 1.92, 95% CI [0.96-3.81], $p = 0.064$; for brain or lymph node, respectively). We observed a trend that patients who had LN metastases without prior brain metastasis had a 33% lower rate of developing subsequent brain metastasis (HR = 0.67, 95% CI [0.44-1.03], $p = 0.071$), while the converse (brain metastasis negatively predicting subsequent development of lymph nodes) was not observed (HR = 1.18, 95% CI [0.79-1.77], $p = 0.42$). Other trends included 1) positive association of peritoneal metastasis and LN metastasis, 2) positive association of brain metastases and both lung and peritoneal metastases, and 3) negative association of adrenal metastasis with liver metastasis. Generally, adrenal metastasis was negatively

associated with subsequent development of metastases at other sites. In contrast peritoneal metastases, a similarly low frequency site, positively associated with development of metastases at other sites. Taken together, our analysis of the effect of site metastasis shows that specific sites associate with survival, total metastatic site burden, and other distant metastatic sites.

Clinico-genomic correlates of metastatic potential:

To explore overall dynamics of metastasis among all patients, we analyzed the mean number of metastatic sites across the cohort over time, utilizing the first radiographic evidence of cancer as time zero (Fig. 3a, Methods). At time zero, patients had a mean of 1.3 metastatic sites, and at 84 months, a mean of 4.3 metastatic sites. To analyze features that associated with different rates of acquiring metastatic sites, we developed a multivariable Andersen-Gill hazard model including sex, age, and TMB as covariates (Fig. 3b-c). Higher TMB and female sex were associated with 32% and 18% lower rates of new metastatic sites, respectively (HR = 0.68 per log10(TMB), 95% CI [0.58-0.8], $p < 0.001$; HR = 0.82 for female sex, 95% CI [0.73-0.92], $p < 0.001$, respectively). Age was not associated with a difference in rate of overall metastatic site acquisition. Next, we assessed the impact of functional gene mutations on the rate of new metastatic sites (Fig. 3d). In univariable analysis, patients with *B2M*, *RB1*, or *PTEN* mutated tumors exhibited a significantly higher rate of new metastatic sites, whereas patients with *EP300* mutated tumors exhibited a significantly lower rate of new metastatic sites (Fig. 3d-e). With B2M being previously implicated in response to systemic therapy, we investigated the treatment history of patients with B2M mutations[22]. Interestingly, *B2M* mutations were detected both before and after systemic therapy, suggesting that *B2M* mutations can have a treatment independent association with broad metastatic potential (Supp Fig. 3a-b).

Patterns of metastasis

Having characterized metastatic frequencies and identified features of overall metastatic potential, we then investigated whether there were larger patterns of site metastasis. We clustered patients by lifetime metastatic site status using a Bernoulli mixture model and selected five clusters based on AIC and median silhouette scores, observing strong evidence of clustering structure (empiric p-value of silhouette score < 0.001, Methods, Fig. 4a, Supp Fig. 4a-d).

The clusters were distinguished by metastatic burden (defined by number of metastatic organs) and dominant sites. The "HM" cluster (highly metastatic) contained 23% of the cohort, was distinguished by high metastatic burden (mean of 5.33 metastatic sites). The "Liver-avid" (high liver) cluster contained 11% of patients and was defined by the presence of liver metastasis, along with a high frequency of bone, LN, and lung metastases (mean of 3.78 metastatic sites). The "Brain-avid" (high brain) cluster contained 22% of patients and was defined by the presence of brain metastasis and low metastatic burden (mean of 2.4 metastatic sites). The "Lung-avid" (high lung) cluster contained 26% of patients and was defined by lung metastasis and low metastatic burden (mean of 1.97 metastatic sites). Finally, the "LM" (low metastasis) cluster contained 18% of patients and was defined by the presence of lymph node metastasis and especially low metastatic burden (mean of 1.55 metastatic sites).
Interpretability and stability of these clusters was reinforced by examining how patients

were distributed into clusters as the number of clusters increased using a “cluster tree.” We found that k=2 separated patients into the highly metastatic and low metastatic distinction, while at k=3 the brain-avid subset of patients emerged and remained relatively stable at all higher values of k (Supp Fig. 4e-f). At k=4, the lung-avid group appeared as a subset of the low metastatic patients, and then at k=5 the liver-avid cluster mainly came from a subset of the highly metastatic patients. Overall, the major clusters we describe remained stable at larger numbers of clusters, and they naturally followed as offshoots of the broadly high or low metastatic groups.

Next, we sought an orthogonal dataset to validate the observed patterns. We analyzed an independent cohort of 5,124 patients with metastatic cutaneous melanoma (Flatiron cohort) whose lifetime metastasis site status was annotated using a different methodology (Methods). Notably, follow up time in this cohort was shorter than our DFCI cohort (median 12, stdev 30.8 months vs. median 18.7, stdev 31.6 months respectively) with concordantly fewer metastatic sites (mean of 2.24 vs. 2.97 metastatic sites among the shared annotated sites respectively). Clustering patients from this independent cohort using the same methodology fell into the same broad categories: highly metastatic, liver/bone-avid, brain-avid with low other sites, lung-avid, and low metastasis, with a few differences (e.g. overall a lower frequency of metastatic sites, including adrenal, peritoneal, and bone metastases) (Fig. 4b, Supp Fig. 5a-e). To test if these independent cohort clusters were concordant with the original clusters, we trained a model to classify patients into the five clusters (Methods) using the discovery cohort data, then used the model to classify patients from the Flatiron cohort into these clusters (Supp Fig. 5f, Methods). We found strong associations between the similarly labeled clusters (e.g. OR for the lung-avid cluster in the independent cohort to the lung-avid cluster in the original cohort = 432.6, $p < 0.001$, Supp Fig. 5g), suggesting strong similarities in clustering structure.

Genetic and clinical features of metastatic clusters

We then compared clinical features between our metastatic clusters. Age and TMB were significantly different between clusters (Kruskal-Wallis $p = 0.0097$, Kruskal-Wallis $p < 0.0001$ respectively, Fig. 4c-d). The Lung-avid cluster contained the oldest patients. The Brain-avid and Lung-avid clusters had the highest TMB (median 16.7/17.5 mutations/MB, respectively), while the HM cluster exhibited the lowest TMB with a median of 10.9 Mt/Mb. We observed a trend that patients in the HM and Liver-avid clusters were more likely to be male compared to the other clusters (Fisher Exact $p = 0.0502$, OR = 1.54) (Fig. 4e). The HM and Liver-avid clusters had more imaging reports and longer follow-up (Supp Fig. 6a-c). To ensure cluster phenotypes were not confounded by these differences in follow-up, we performed landmark analysis of total metastatic sites at 12 months and found that the results were consistent with the full follow-up analysis (Supp Fig. 6d). The order of site frequencies within each cluster remained consistent across time (Supp Fig. 6e). The HM and Liver-avid clusters had the worst overall survival across clusters, while the Lung-avid and LM clusters had the longest survival (Supp Fig. 6f-g).

While brain metastases were present in multiple clusters, the characteristics of the brain samples differed. Comparing brain biopsies from patients in the HM and Brain-avid clusters (n = 34, 19, respectively), brain biopsies from patients in the Brain-avid cluster had an approximately 2-fold higher TMB than brain biopsies from patients

in the HM cluster (median 28.7 vs 10.9 respectively, Wilcox p = 0.016, Fig. 4f).

Next, we tested if functional gene mutations were enriched in any cluster (Methods) (Fig. 4g). Mutations in *BRAF* and *PARK2* were significantly enriched in the low metastatic cluster. Mutations in *NF1* were significantly depleted in the HM cluster. Mutations in *CBL* were significantly enriched in the Liver-avid cluster. Interestingly, mutations in *B2M*, which were associated with increased overall metastatic potential, were mutually exclusive with the Brain-avid and LM clusters (OR = 0, both 95%, p = 0.05 and = 0.085, respectively).

Clinical and Genomic Associations of site-specific metastasis

Moving from broad metastatic potential and patterns, we investigated features associated with site-specific metastasis. To address this question, we analyzed clinico-genomic predictors of longitudinal site-specific time-to-metastasis (Methods).

Broadly, results were consistent with prior associations of female sex and higher TMB with decreased overall metastasis (Fig. 5a). The strongest effect sizes of female sex and high TMB were observed with decreased rates of liver metastasis (cause-specific hazard ratio (CSHR, Methods) of 0.62 and 0.40, 95% CI [0.44-0.87] and [0.24-0.66], p = 0.005 and < 0.001, respectively). Interestingly, age was not associated with overall differential metastatic rates holding sex and TMB constant, but it was significantly associated with increased rates of lung and adrenal metastases (7% and 9% increased rate of metastasis per 5 years of age, p=0.002 and 0.03, respectively). Highlighted cumulative incidence curves are plotted in Fig. 5b. Interestingly, we observed that in some cases, a threshold value of TMB seemed to distinguish patients with different rates of site-specific metastasis; the highest quartile of TMB separated from the other three quartiles with the lowest adrenal metastasis rate, while the lowest quartile of TMB separated from the other quartiles with the highest rate of peritoneal metastasis (Fig. 5b).

We then tested whether functional mutations in genes were associated with a change in the risk of specific metastatic sites. Using a cause-specific hazard model with a time-dependent covariate of total metastatic sites, we analyzed gene mutations associated with site specific incidence of metastasis (Fig. 5c). To test robustness of our results, we tested a different survival model (subdistribution, Methods) and different choices of reference times (i.e. setting time zero to be the time of sequenced biopsy), and observed consistent results (Methods, Supp Fig. 7). Looking at the results across all sites, we highlighted specific associations of interest (Fig. 5d, Supp Fig. 8). We observed that loss-of-function mutations in *PTEN* were associated with increased incidence of brain metastasis (SDHR = 1.7, 95% CI [0.98-2.92], p = 0.057; CSHR = 1.74, 95% CI [1.01-3.0], p = 0.046; adjusted CSHR = 1.82, 95% CI [1.06-3.12], p = 0.044), consistent with previous literature linking *PTEN* with brain metastasis in melanoma[23]. Next, we observed broad site-specific associations with loss-of-function mutations in *B2M*, with higher incidence of metastasis in LN (SDHR = 1.74, 95% CI [1.21-2.49], p < 0.01), liver (SDHR = 2.0, 95% CI [1.06-3.78], p < 0.05), and lung (SDHR = 1.8, 95% CI [1.34-2.4], p < 0.01).

To validate these associations, we tested select significant results in an independent cohort of patients with cutaneous melanoma from a different institution (MSK, Methods). Notably, we recapitulated associations of liver, LN, and lung metastasis with *B2M* (Supp Fig. 3c-d). Overall, by using longitudinal models of

metastasis, we identified site-specific associations with both clinical features and genomic alterations.

GNA11/GNAQ mutations confer risk of liver metastasis in patients with cutaneous melanoma

We observed that gain-of-function alterations in *GNA11* and its paralog *GNAQ* were associated with increased incidence of liver metastasis with similar effect size (SDHR = 2.94, 95% CI [1.29-6.72], p = 0.01; SDHR = 2.87, 95% CI [1.1-7.5], p = 0.03 respectively). Using the independent cohort of patients with cutaneous melanoma described in the previous section (MSK), we recapitulated associations with liver metastasis and GNA11/GNAQ (Fig. 6a-b). Since *GNA11* and *GNAQ* are known paralogs and since driver mutations in these genes were mutually exclusive among our patients (and in other cancers), we combined the two groups of mutated patients into a single subgroup. This combined *GNA11*/*GNAQ* subtype had a large increase in incidence of liver metastasis (CSHR = 3.1, 95% CI [1.44-6.59], p = 0.004; SDHR = 3.01, 95% CI [1.59-5.7], p < 0.001) (Fig. 6c).

Since uveal melanomas are driven by mutations in *GNA11* or *GNAQ* and canonically metastasize to the liver[24], we hypothesized that *GNA11* and *GNAQ* mutations in cutaneous melanoma may confer a tumor-intrinsic propensity for liver tropism. To do this, we verified that these melanoma tumors were of cutaneous origin. First, we reviewed the clinical history of these patients, confirming that these patients did in fact have cutaneous melanoma diagnoses and were not misclassified or had concurrent uveal melanoma. Second, these GNA11/GNAQ mutant cutaneous melanoma tumors had TMB levels consistent with cutaneous melanoma and significantly higher than uveal melanoma (Fig. 6d). Third, we characterized other clinical and genomic features of these patients (Fig. 6e). Of the 9 tumor samples, 5 were primary skin biopsies (consistent with cutaneous melanoma etiologies), 1 sample from head-neck, and 3 samples were brain biopsies. A UV mutational signature was detected in 5 of the 9 tumor biopsies. Of the 4 tumors without called UV signatures, 3 were characterized by a low number of SNVs which may have limited the ability to call the signature. Looking at the co-occurrence of other mutations, 2 patients had *NF1* mutations, 1 had a *BRAF* mutation, and 1 had an *NRAS* mutation, uncommon in uveal melanomas[24]. Other typical genes mutated in uveal melanoma such as *SF3B1*, *BAP1* were only seen in one of ten tumors. Lastly, four patients had a peritoneal metastasis in their disease history, a location less characteristic of uveal melanoma[25].

Thus, clinical and genomic characterization confirmed that these tumors had clinical and genomic characteristics of cutaneous melanoma, and this, along with validation in an independent dataset, gives us confidence in our observation that cutaneous melanoma patients with *GNA11/GNAQ* mutations exhibit high rates of liver metastasis.

Liver tropism of Gnaq/Gna11-driven cutaneous melanoma in genetically engineered mouse models

To examine whether the association between metastatic organotropism and driver mutations was also observed in pre-clinical models, we compiled the known alleles and

sites of spontaneous metastases (Table 1) of previously described genetically engineered mouse (GEM) models of cutaneous melanoma. Specifically, we selected models where spontaneous sites of metastasis were assessed after the primary melanoma was initiated (following genetic activation and/or carcinogenic treatment) and the tumor was genomically characterized for driver mutations.

In these experimental model systems, whereas *Braf* and *Ret*-driven models were dominated by lung metastases, *Hras*-driven models with or without carcinogen treatment were dominated by lung and lymph node macrometastases with lesions at other sites mostly micrometastases. In contrast, liver metastases appeared more frequently in *Nras*- and *Gnaq*-driven models and *Hgf*-transgenic (tg) melanoma models. We have previously identified frequently mutated Q209 hotspots within *Gnaq/Gna11* in *Hgf*-transgenic melanoma[26] which are consistent with the human data that *Gnaq/Gna11* mutations in melanoma are associated with liver metastasis.

We then evaluated the liver organotropism of a *Gna*-mutant melanoma (Fig. 7a) using C5, a GEM-derived allograft (GDA) line of cutaneous melanoma with *Gna11*^{Q209L} and *Trp53*^{R172H} mutations, generated from a DMBA-induced melanoma in a *Hgf-tg;Cdk4*^{R24C} C57BL/6 genetic background[26,27] (Supp Fig. 9a). We labeled the C5 cells with firefly (ff) luciferase/H2B-GFP genes *ex vivo* (Methods) to enable bioluminescence imaging (BLI) for monitoring disease progression and then implanted into a syngeneic mouse for tumor expansion[28]. In a representative study, the grown tumor was then transplanted subcutaneously into five syngeneic hosts (Fig. 7b). After the primary tumors were resected upon reaching 500 mm^3, mice were monitored by BLI for metastasis. Three of five mice developed macrometastases in liver, and one out of five had macrometastases in lung (Fig. 7c-d; confirmed by necropsy reports). Noticeably, the metastatic burden in liver was significantly higher than those in lung.

In a parallel study, we tested whether tumors that had metastasized to one site could retain tropism to the liver. We harvested metastatic nodules from the lung or liver of the mice implanted with labeled C5 tumor, and then transplanted them subcutaneously into recipient mice, respectively, followed by monitoring metastasis by BLI after resection of the primary tumors. We observed that subcutaneous implants from liver metastases (Fig. 7e) and lung metastases (Fig. 7f) both resulted in similar metastatic phenotypes with high frequency metastases in the liver and lung and particularly high-burden metastases in the liver. Repeat experiments showing the robustness of this phenotype across implants from liver metastases, lung metastases, and subcutaneous primaries are summarized in Supp Fig. 9c-d, suggesting that the liver tropism is an intrinsic feature of this *Gna11*-mutant model.

Finally, we implanted a Gnaq^{Q209L}-driven melanoma GDA derived from UV-irradiated Hgf-tg;Cdkn2a$^{+/-}$ mice into syngeneic C57BL/6 mice and resected the primary tumors upon reaching 500 mm3 in a similar protocol (Methods). At the protocol-defined endpoint, the mice were euthanized for necropsy, and the organs were harvested for fixation. Across experiments, there was a large burden of liver metastases, high frequency of lung metastases, and variable metastases across other sites (Fig. 7g).

Taken together, these results demonstrated liver tropism of *Gna11/Gnaq*-mutated melanoma metastasis in an immunocompetent mouse model and offers a possible model by which to test further mechanisms or interventions.

Discussion

In this study, we performed in-depth analyses of clinico-genomic cohorts of cutaneous melanoma patients with longitudinal metastatic annotations. We characterized metastasis on multiple levels, including overall metastatic potential, recurrent patterns of metastasis, and site-specific metastases, and we elucidated their associated clinical features and function genomic alterations, thereby expanding upon prior discoveries and making novel and higher-resolution observations of the patterns of metastasis in patients and their potential drivers. Our longitudinal approach enabled us to model features that affect the rates of metastasis, and we utilized multiple different competing risk models to evaluate robustness of our findings.

Among clinical factors, we observed that female sex was associated with decreased metastasis overall, which has been previously described[29], and we observed the strongest protective effects in liver, peritoneal, and bone metastasis. While age was not associated with overall metastatic burden, we observed a strong effect of age on increased rates of metastases to the lung and adrenal sites, and the highest age distribution in the Lung-avid cluster of patients. Interestingly, recent work has found that aged lung microenvironments may induce reactivation of dormant melanoma cells and provide a permissive niche for metastasis[30].

We observed a strong association between higher tumor mutational burden and fewer metastases overall, which manifests strongly across all site-specific contexts. Our cluster analysis corroborates this trend, with the highest metastatic burden clusters having patients with the lowest TMB. Interestingly, this was not observed in a prior pan-cancer analysis, though there were trends in both directions in different tumor histologies[11]. In the context of treatment within cutaneous melanoma, higher TMB has been associated with response to immune checkpoint inhibition and longer overall and progression free survival[31], potentially suggesting the role of immune activation and surveillance in limiting broad metastatic potential.

Importantly, we identify and independently validate global patterns of clinical metastasis, with key clinical and biological insights. Patient metastatic clusters are driven by two axes: overall metastatic potential (i.e. low vs high number of metastatic sites), and organotropic metastasis to specific sites (brain, lung, liver). These clusters have distinct clinico-genomic profiles and raise hypotheses that there are distinct biological mechanisms leading to metastasis. Patients with brain metastases in the two clusters had distinct genomic and clinical features; the patients in the brain-tropic cluster were older and their tumors had almost twice the number of mutations compared to patients with highly metastatic tumors. Further, while *PTEN* loss-of-function mutations have been previously shown to associate with brain metastases[11,23,32] (and recapitulated in our cohort (Fig. 5c)), they strongly associated with increased overall metastatic potential (Fig. 3d) and were enriched in the patient cluster defined by high metastatic potential rather than the brain-specific cluster (Fig. 4d), suggesting that the mechanism leading to brain metastasis in *PTEN* mutated melanomas is not unique to the brain microenvironment and leads to metastases at other sites.

Indeed, *PTEN* mutations have been found to be associated with immunosuppressive microenvironments across different histologies, mediated through multiple mechanisms including regulation of immune cell trafficking (VEGFA expression) and autophagy[33–35]. Strikingly, B2M (required for MHC-I antigen presentation to T cells) loss-of-function mutations were also strongly associated with

broad metastatic potential. While in some patients we detected *B2M* mutations in tumor samples after detection of post-treatment resistant tumor samples, consistent with its known role in immune evasion and immunotherapy resistance[36], we also detected *B2M* mutations pre-treatment and development of broad macrometastases. Together, these observations suggest that immune surveillance mediated at least in part by T cells limits metastasis broadly across organ sites.

We find a strong association of *GNAQ/GNA11* gain-of-function mutations with rapid development of liver metastases and validated this association in an independent clinical cohort. Prior literature has described a subset of cutaneous melanomas with *GNA11/Q* driver mutations[37], and multiple lines of evidence (TMB, co-occurring driver mutations, UV mutation signatures, and clinical review) gives us confidence that these are indeed cutaneous melanomas.

Interestingly, *GNAQ/GNA11* mutations drive uveal melanomas (melanomas that arise in the eye), and when these tumors metastasize, they almost always metastasize to the liver. This suggests that GNA11/Q mutations may be associated with a tumor-intrinsic biological state with tropism to the liver. In preclinical models, liver is a rare metastatic site; however, in existing autochthonous (spontaneous) cutaneous melanoma mouse models, liver metastasis was enriched in *Gna11/q* mutant melanomas (Table 1). We further confirm striking and reproducible liver metastasis after flank injection (and survival surgery) of *Gna11*-mutant and Gnaq-mutant cutaneous melanoma mouse models.

Other mechanisms of liver metastatic organotropism have been demonstrated, including PI3K/AKT signaling pathways identified using CRISPR screens, with *PIP4K2C* loss as a metabolic adaptation for metastatic colonization[7]. The mechanism of GNAQ/11 mutations as drivers of liver organotropism are unclear. It was recently observed that *GNAQ*^{Q209L} mutations led to constitutive phosphorylation of MET (receptor for hepatic growth factor, HGF) in an immortalized melanocyte cell line[38], and prior work has implicated the cMet/HGF axis in liver metastasis[39], but whether this is the primary mechanism or whether other pathways co-regulate the process requires further mechanistic studies. Further, non-cutaneous melanomas with GNA-mutations (uveal, CNS[40], and mucosal melanomas[41]) have poor treatment options and prognosis after metastasis. Manual review of two patients with CNS-based melanomas (excluded from the primary analysis) and *GNA11/GNAQ* mutations revealed both ultimately developed liver metastasis, highlighting the potential broader impact of elucidating the relevant mechanisms (and potential therapeutic targets) across multiple hard-to-treat diseases.

Several limitations exist for this study. First, despite being a major site of metastasis in cutaneous melanoma, soft tissue metastases were not annotated in the NLP model used in the discovery cohort and therefore not included in our analysis. Next, artificial intelligence annotations allow for higher throughput data curation, but the models may create systematic artifacts due to clinical edge cases or complex clinical histories. Despite this, the model derived annotations performed extremely well in our manual validation of patient annotations, and our manual review of highlighted findings give us confidence that they are not due to miscalled annotations. Further, validation of metastatic patterns and genomic drivers associated with metastatic phenotypes in independent cohorts with different sequencing panels and methods of inferring metastatic phenotypes from clinical records gives us confidence in these findings.

A fundamental limitation is that genomic sequencing was obtained from a single

biopsy in the vast majority of patients; an implicit assumption in our analyses is that the genomic characteristics are consistent over time in the same patient, though multiple prior studies of matched tumor samples have shown that driver mutations are largely maintained between tumors[42]. Despite the size of our cohort, the relevant group sizes decrease quickly when we consider specific covariates (e.g. functional gene mutation, treatment, metastatic cluster), and larger cohorts would improve our power to detect these types of relevant effects. Our validation of specific genomic findings in an independent cohort mitigates this, but further validation in other large, independent cohorts will be necessary, in addition to functional studies to further characterize the biological mechanisms underpinning our observations. Lastly, differences in treatment were not explored in this study, but certainly may impact metastatic outcomes or tumor evolution.

Taken together, our study presents a comprehensive, integrative, and novel analysis of clinical organotropism in cutaneous melanoma, providing insight into the patterns and drivers of metastasis. We nominate novel mechanisms of site-specific metastasis, laying the foundation for further studies to dissect these mechanisms and identify targets to interrupt the metastatic process. Broadly, our study provides a framework for deriving biological insights about the heterogeneity of metastasis in patients that can be easily translated to other cancer histologies.

Tables

Table 1. Spontaneous metastasis from the autochthonous cutaneous melanoma generated in the genetically engineered mouse models.

Model	Carcinogen	Metastatic sites (occurrence rate)	Reference (PMID)	Year
Dct::TVA;Braf^{CA};Cdkn2a$^{lox/lox}$;Pten$^{lox/lox}$		Lung (8.3%)	26565903	2015
Dct::TVA;Braf^{CA};Cdkn2a$^{lox/lox}$;Pten$^{lox/lox}$ + MyrAkt		Lung (67%), brain (17%)	26565903	2015
Braf$^{+/LSL-D594A}$;Kras$^{+/LSL-G12D}$;Tyr::CreERT2		Spleen (20%)	24667377	2014
Tyr::Cre^{ERT2}; Braf$^{CA/+}$; Pten$^{fl/fl}$; Bcat-STA		Lung (100%), Bowel (60%), Spleen (10%)	22172720	2011
Tyr::Cre^{ERT2}; Braf$^{CA/+}$; Pten$^{fl/fl}$		lung/LN (100%)	19282848	2009
Tyr::Hras^{G12V}Cdkn2a$^{-/-}$; Pten$^{+/-}$		rare LN, lung	20711233	2010
Tyr::Hras^{G12V}Cdk4$^{R24C/R24C}$	UV	LN	16540642	2006
Tyr::Hras^{G12V}	UV+DMBA/TPA	LN, lung (50%)	10469620	1999
Tyr-CRE-ER^{T2}p16$^{L/L}$LSL-Nras$^{Q61R/Q61R}$; Lkb1$^{fl/fl}$		Lung*, spleen*, liver*, LN	25252692	2014
Tyr::Nras^{Q61K}; p16$^{-/-}$		LN (36%), lung*, liver*	15899789	2005
Tyr::Nras^{Q61K}; p16$^{-/-}$		Lung, liver, brain (at any site overall 43%)	22109529	2011
MT::HGF ± Cdk4$^{R24C/R24C}$	DMBA+TPA	LN, lung	16877364	2006
MT::HGF;Cdk4$^{R24C/R24C}$	UV	LN (100%), lung (80%), liver (10%)	21207411	2011
MT::HGF; Cdkn2a$^{-/-}$	UV	LN, liver	12438273	2002
MT::HGF		Liver (100%), lung (100%), spleen (43%), ovary (14%), LN (14%),	9823327	1998
MT::RET(human); Ednrb$^{+/-}$		lung (~40%)	20048069	2010
MT::RET(human)	UV	Lung (50%)	11121157	2000
MT::RET(human)		LN* (52%), lung, brain* (44%), liver* (12%), kidney* (12%)	9778055	1998
Mitf-cre/+; R26-fs-GNAQ$^{Q209L/+;}$ Bap1$^{KO/+}$ *Mitf-cre/+; R26-fs-GNAQ$^{Q209L/+;}$ Bap1$^{fl/+}$*		Liver (20%, 40%, respectively)	(Fagun Jain Master thesis)	2016
Dct::Cre; Pten$^{fl/fl}$	DMBA+TPA	Lung (20%)	18632629	2008
P16$^{-/-}$;p19$^{+/-}$	DMBA	LN*, lung, liver* spleen* (at any site overall 37.5%)	11544530	2001
Dct::Grm1		LN (100%)	12704387	2003
Cdh23$^{ahl/ahl}$	DMBA	LN, lung (at any site overall 8%)	11479419	2001
Tyr::SV40E	UV	LN, lung, kidney	9751610	1998

* Micrometastases or small lesions.
LN: Lymph node

Methods

Patient cohort, Processing, QC, Manual

We identified 881 patients with melanoma tumor NGS panel data generated between 2005-2022 and whose imaging reports were annotated by the NLP model. Using the model results from Kehl 2021[13], we assembled a dataset of 26,117 artificial intelligence-annotated text imaging reports from 881 patients. Annotated imaging reports were filtered according to multiple criteria. Model predictions included presence of cancer, progression/response, worsening/improvement, and the presence of various metastatic sites. Possible sites of metastasis that were annotated included brain, bone, lymph node, lung, liver, adrenal gland, and peritoneal. No distinction was made between distant and regional lymph node metastasis. All patients were evaluated at the Dana-Farber Cancer Institute, and each patient had at least one tumor biopsy sequenced with OncoPanel, a next-generation DNA sequencing panel that identifies mutations in cancer-related genes[19]. Biopsy site of sequencing varied by patient, and no requirement was made for cohort inclusion. The melanoma cohort was limited to those patients with cutaneous melanoma (N=603). Patients with melanoma and an unknown primary site were included as cutaneous if they had evidence of cosmic[43] mutational signature 7 (ultraviolet exposure) (N=142, filtered to N=74). Upon manual review, we removed one patient due to having a meningeal melanoma and removed another patient for having a spinal melanoma. Multiple criteria were used for both patient and scan inclusion. Scans were limited to those that were annotated as having a presence of cancer by the NLP model, along with being an MRI, CT, or PET scan. This was done to limit annotations to more accurate and task-specific scans. Patients were included if they had at least one scan that passed these criteria, thus having radiographic evidence of cancer. This resulted in a total of 598 patients with cutaneous melanoma.

Lastly, we limited our cohort to patients who developed metastatic cutaneous melanoma by examining the disease extent of patients at first radiographic evidence of cancer. Patients who did not have metastatic disease at this point, and did not have a metastatic site predicted in the follow-up period, were excluded for not having sufficient evidence of ever having metastatic melanoma. We implemented a time cutoff of 84 months to limit timespan of metastatic development to relevant follow-up periods, retaining the full follow-up for over 90% of patients. No minimum follow-up was required for cohort inclusion. For quality control, we evaluated the performance of the NLP metastatic annotations on a subset of 66 melanoma patients with manual annotations from radiographic reports within 4 months prior to systemic immunotherapy treatment. Within this time range, the NLP model performed well across the metastatic sites, with median sensitivity and specificity of 0.88 and 0.94, respectively (Supp Fig. 2a-b).

DNA sequencing and Functional Annotation

All patients included in the cohort had OncoPanel targeted panel sequencing for at least one melanoma biopsy, allowing identification of tumor somatic alterations[19]. These samples consisted of three versions of OncoPanel Sequencing, with the number of sequenced genes differing between them. Version 1 sequenced 275 genes (n=19), version 2 sequenced 300 genes (n=79), and version 3/3.1 sequenced 447 genes (n=374). To ensure fair comparison across samples, we limited to only genes that were shared across all versions on OncoPanel. This led to 239 genes of interest. Gene

level somatic mutations were filtered for functional impact using the OncoKB database[44]. Alterations annotated with oncogenic levels of "Likely Oncogenic", "Oncogenic", "Resistance" or annotated with mutation effect of "Gain-of-function", "Likely Gain-of-function", "Likely Loss-of-function", "Likely Switch-of-function", "Loss-of-function", "Switch-of-function" were included as being functionally relevant. After gene level filtering, 158 genes still had at least 1 functional alteration across the cohort. When patients had more than one sequenced sample (17 patients), mutation status for genes were aggregated across all sequenced biopsies. Thus, mutation status in a gene indicates whether a patient had a functionally relevant mutation in that gene across any of their available sequenced biopsies. Tumor mutational burden estimates were also averaged across all samples for patients with multiple samples. Finally, genes included in statistical testing were limited to those that were altered in at least 3 patients across the cohort, leading to 96 genes analyzed in this study. For more interpretable testing of genomic associations, we categorized alterations in genes as loss-of-function (LOF), gain-of-function (GOF), or other based on the OnkoKB annotation details.

For mutation signature calling, we used *deconstructSigs* (v1.8.0). Signatures were from the single base substitution signatures found in the Catalog of Somatic Mutations in Cancer (COSMIC) database[43].

Survival modeling

Time to event analysis was set up as follows: Start time was defined as the date of the first scan predicted to have evidence of cancer based on NLP model annotations of imaging reports. Time of metastasis was defined as the date of the first imaging report predicted positive for each site. Patients who did not have a site in the follow-up time were censored, and those who died were marked for the competing event. For overall survival estimation, we used the Kaplan-Meier method, and to model the effect of covariates on survival we used a Cox proportional hazard model. We used cause-specific hazard and subdistribution hazard models to account for competing events and determine the effect of covariates on metastasis. Cause-specific models were run in R using *coxph* from the *survival* (v3.5-7) package, with death being marked as a censoring event. Penalized cause-specific models using Firth's penalized likelihood for Cox regression were run in R using *coxphf* from the *coxphf* (v1.13.4) package, with death again marked as a censoring event. The penalized model was used to account for cases of complete separation. Subdistribution hazard models were run in R using *crr* from the *tidycmprsk* (v0.2.0) package, with death coded as a competing event. For estimation of mean cumulative functions, we used the *mcf* function from the *reda* (v0.5.4) package. We used Andersen-Gill models for modeling new metastatic sites as recurrent events. Andersen-Gill models were run in R using *coxph* with the general format: *coxph(Surv(tstart,tstop,metastasis)~covariate, cluster=ID, ...)*. Time dependent covariates of either total metastatic sites or site-specific incidence were created using the *tmerge* function from the *survival* package and were included as mentioned for certain models.

Unsupervised clustering and assessment

Bernoulli mixture models were estimated using the R *flexmix* package (v2.3-19)[45]. We clustered patients by their status for metastatic sites in the follow-up period. For each value for k components (ranging from 1-7), we ran 1,000 random initializations for 500 maximum iterations. The expectation maximization would stop when the change of log-likelihood was smaller than $1x10^{-6}$ and kept the model with the maximum likelihood. We calculated Akaike information criterion (AIC) and silhouette scores for each value of k components, noting that the minimum AIC was at 4 mixture components, with similar results for neighboring values (Supp Fig. 4a), while there was a large increase in median silhouette score from 4 to 5 components (Supp Fig. 4b-c). Due to this substantial increase in median silhouette score with a minimal change in AIC, we decided to use k=5 components for the final Bernoulli mixture model.

To test how the estimated clusters compared relative to a random dataset with no association between metastatic sites, we generated 1000 random site occurrence datasets by permuting our observed site data to create a null distribution of median silhouette scores for a k=5 Bernoulli mixture model. Using this null distribution, we generated significant empirical p-values for the metric from our observed data (Supp Fig. 4d).

To further explore how the structure of the clusters fluctuated with different component numbers, we plotted the frequency of metastatic sites across clusters for the optimal model at each value of k (Supp Fig. 4e). We further created a cluster tree showing the movement of patients between clusters at different numbers of components (Supp Fig. 4f), observing clear presence of similar cluster characteristics at both lower and higher numbers of components, but a low degree of inter-cluster movement past 5 components.

To test for enrichment of mutations in any cluster, we performed Fisher exact tests for whether a patient's tumor had a functional mutation in each gene with whether a patient is in one cluster vs any other.

To classify patients into clusters, we calculated the posterior class probabilities for each cluster by using the baseline frequency of each cluster as the prior probability and using site frequencies to calculate the likelihood of observing those metastatic sites given a cluster[45]. To account for cases where the site frequency of a cluster is 0, a weight is added to make the posterior probabilities defined. We then assign patients to the cluster with the maximum posterior probability.

Validation Cohorts

We utilized two validation cohorts of patients with cutaneous melanoma.

For our cluster validation cohort, we utilized the nationwide, longitudinal Flatiron Health database, an electronic health record-derived database comprising deidentified patient-level structured and unstructured data, curated via technology-enabled abstraction from approximately 280 cancer clinics (~800 sites of care) in the United States[46,47]. The majority of patients in the database originate from community oncology settings; relative community/academic proportions may vary depending on study cohort. The data are deidentified and subject to obligations to prevent reidentification and protect patient confidentiality. Institutional review board approval was obtained prior to conducting the study (IRB#2000036075). Patients with metastatic melanoma treated in the front line setting with immunotherapy (ipilimumab + nivolumab, anti-PD1 monotherapy,

or nivolumab + relatlimab) or BRAF/MEK inhibitors were included (n=5,124). Patients without documented metastatic sites or overall survival data were excluded.

For genomic validation, we utilized a cohort of 1,801 patients with cutaneous melanoma with MSK-IMPACT targeted tumor sequencing[48] and NLP derived longitudinal metastatic annotations for all sites of interest except peritoneum[10].

Mouse models of metastatic Gnaq/Gna11-mutated cutaneous melanoma.

GEM-derived allograft (GDA), C5, was generated from a Hgf-tg;Cdk4^{R24C} C57BL/6 mouse following DMBA treatment, as described previously[26]. Additional mutations were characterized by exome sequencing, including Gna11^{Q209L} (Supp Fig. 9b). The generation of firefly (ff) Luc-eGFP-labeled C5 GDA has been described previously[28]. Briefly, the C5 GDA was transplanted into syngeneic C57BL/6 mice subcutaneously. Harvested C5 tumors from the transplanted hosts, mixed with culture medium containing lentivirus of FerH-ffLuc-IRES-H2B-GFP (IRES, internal ribosome entry sequence; H2B-GFP, Histone 2B-tagged green fluorescence protein). Following transduction by spinoculation[49], the medium was removed, and the cells were subcutaneously transplanted into albino C57BL/6$^{cbrd/cbrd}$ glowing head (cbrd GH) mice pre-tolerized with ffLuc and GFP[28].

To test the metastatic potential, ff Luc/H2B-GFP-labeled C5 tumors were transplanted into cbrd GH mice subcutaneously. Once the primary tumors reached a size of 500mm3, tumors were surgically resected and mice monitored via bioluminescence (BL) using the Xenogen IVIS system[49]. At the endpoint defined by the sickness behavior and moribund status, the mice were euthanized for necropsy, and the organs were harvested for BLI imaging ex vivo.

In another GEM model, melanoma was induced in Hgf-tg;Cdkn2a$^{+/-}$ mice by UV irradiation at neonatal day 3. The procedure was described previously except that the mouse strain background used in this study is C57BL/6[50]. One of the melanoma tumors was harvested from a donor mouse and transplanted into syngeneic recipient for expansion and further passage as GDA (Fig. 7g). The endpoint was also defined by the sickness behavior and moribund status.

Statistical analysis and visualization

All statistical analyses were performed in R (v4.2.1 "Funny Looking Kid"). For the comparison between continuous clinical and molecular features, the Mann-Whitney test was used. For association of binary variables, Fisher's exact test was used. Reported p-values represent nominal p-values unless otherwise stated. All statistical tests performed were two-sided unless otherwise stated.

Visualizations were created with the R packages *ggplot2* (v3.4.2), *cowplot* (v1.1.1), *ggpubr* (v0.6.0), *ComplexHeatmap* (v2.14.0), *survminer* (v0.4.9), and *tidycmprsk* (v0.2.0). The Adobe Illustrator software was used to arrange figures.

Declarations

Funding

This research was supported by the Intramural Research Program of the National Cancer Institute (C.P.D.), the National Institute of Health (K08 CA234458, U2CCA233195; D.L.), and the Doris Duke Clinical Scientist Development Award (D.L.).

Conflict of interest/Competing interest

R.H. reports advisory/consulting with Immunocore and research funding from Pfizer and Novartis. K.L.K reports research funding from Meta. J.J.I. reports the following relationships: personal fees from Related Sciences (consulting), Danger Bio (consulting/equity), Phenomic AI (consulting / equity), Kronos Bio (equity) and grants from AstraZeneca (sponsored research agreement) outside of the submitted work. A.N.S. reports advisory board / personal fees with Bristol-Myers Squibb, Immunocore, Novartis, and Erasca, along with trial support to institution from Bristol-Myers Squibb, Immunocore, Novartis, Targovax, Pfizer, Alkermes (Mural Oncology), Checkmate Pharmaceuticals, Foghorn Therapeutics, Linnaeus Therapeutics, Lovance Biotherapeutics, Obsidian Therapeutics. F.S.H reports grants and personal fees from Bristol-Myers Squibb, personal fees from Merck, grants and personal fees from Novartis, personal fees from Compass Therapeutics, personal fees from Apricity, personal fees from Bicara, personal fees from Checkpoint Therapeutics, personal fees from Genentech/Roche, personal fees from Bioentre, personal fees from Gossamer, personal fees from Iovance, personal fees from Catalym, personal fees from Immunocore, personal fees from Kairos, personal fees from Rheos, personal fees from Bayer, personal fees from Zumutor, personal fees from Corner Therapeuitcs, personal fees from Puretech, personal fees from Curis, personal fees from Astra Zeneca, personal fees from Pliant, personal fees from Solu Therapeutics, personal fees from Vir Biotechnology, personal fees from 92Bio, outside the submitted work; In addition, Dr. Hodi has a patent Methods for Treating MICA-Related Disorders (#20100111973) with royalties paid, a patent Tumor antigens and uses thereof (#7250291) issued, a patent Angiopoiten-2 Biomarkers Predictive of Anti-immune checkpoint response (#20170248603) pending, a patent Compositions and Methods for Identification, Assessment, Prevention, and Treatment of Melanoma using PD-L1 Isoforms (#20160340407) pending, a patent Therapeutic peptides (#20160046716) pending, a patent Therapeutic Peptides (#20140004112) pending, a patent Therapeutic Peptides (#20170022275) pending, a patent Therapeutic Peptides (#20170008962) pending, a patent THERAPEUTIC PEPTIDES Therapeutic Peptides Patent number: 9402905 issued, a patent METHODS OF USING PEMBROLIZUMAB AND TREBANANIB pending, a patent Vaccine compositions and methods for restoring NKG2D pathway function against cancers patent number: 10279021 with royalties paid, a patent antibodies that bind to MHC class I polypeptide-related sequence A patent number: 10106611 issued, a patent ANTI-GALECTIN ANTIBODY BIOMARKERS PREDICTIVE OF ANTI-IMMUNE CHECKPOINT AND ANTI-ANGIOGENESIS RESPONSES Publication number: 20170343552 pending, and a patent Antibodies against EDIL3 and methods of use thereof pending.
All remaining authors have declared no conflicts of interest.

Ethics approval

This retrospective study and associated informed consent procedures were approved by the central Ethics Committee (EC) of the Dana Farber Cancer Institute (IRB 20-684 and 16-360). Approval by the local EC was obtained by investigators if required by local regulations.

All mouse experiments were performed in accordance with Animal Study Protocols (11-044 and 11-007) approved by the Animal Care and Use Committee, NCI-Frederick, NIH. NCI is accredited by the Association for Assessment and Accreditation of Laboratory Animal Care and follows the Public Health Service Policy on the Care and Use of Laboratory Animals. All animals used in this research project were cared for and used humanely according to the following policies: the US Public Health Service Policy on Humane Care and Use of Animals; the Guide for the Care and Use of Laboratory Animals (2011); and the US Government Principles for Utilization and Care of Vertebrate Animals Used in Testing, Research, and Training (1985).

Material availability

Further information and requests for resources and reagents should be directed to and will be fulfilled by D.Liu as corresponding author. Requests for reagents derived from mouse models (alleles, tumor tissue, cell lines) developed in this study will require a material transfer agreement as per NIH guidelines.

Code availability

Software environments and code to reproduce all analysis and generate figure plots is available at GitHub at (https://github.com/davidliu-lab). Additional reasonable requests for code will be promptly reviewed by the senior authors to verify whether the request is subject to any intellectual property or confidentiality obligations and shared to the extent permissible by these obligations.

Data availability

All data necessary for figure generation are in supplementary tables or data available on GitHub at (https://github.com/davidliu-lab). Any reasonable requests for raw and analyzed data and materials will be promptly reviewed by the senior authors to determine whether the request is subject to any intellectual property or confidentiality obligations. Patient-related information not included in this paper may be subject to patient confidentiality.

Authors' contributions

T.J.A and D.Liu conceived and designed the overall study. C.D. performed mouse experiments and contributed manuscript sections. T.J.A., G.T. acquired and processed data, and/or performed data analysis. Z.W and R.E assisted with data acquisition. M.M., H.F., M.M.H., K.Khaddour, and C.F. assisted with clinical annotation and data acquisition. D.Lee, A.P., J.I. performed validation of clustering results and interpreted data. J.J., N.S., A.S., performed validation of genomic results. G.T., M.Glettig, and K.P.B. interpreted data. K.Kehl., M.Griffith, A.G., J.I., K.P.B., F.S.H, and R.H. contributed key discussions. T.J.A. and D.Liu interpreted the data and wrote the manuscript. All authors reviewed and edited the manuscript.

References

1. Gerstberger, S., Jiang, Q. & Ganesh, K. Metastasis. *Cell* **186**, 1564–1579 (2023).
2. Paget, S. The distribution of secondary growths in cancer of the breast. 1889. *Cancer Metastasis Rev.* **8**, 98–101 (1989).
3. Gao, Y. *et al.* Metastasis Organotropism: Redefining the Congenial Soil. *Dev. Cell* **49**, 375–391 (2019).
4. Valastyan, S. & Weinberg, R. A. Tumor Metastasis: Molecular Insights and Evolving Paradigms. *Cell* **147**, 275–292 (2011).
5. Massagué, J. & Ganesh, K. Metastasis-Initiating Cells and Ecosystems. *Cancer Discov.* **11**, 971–994 (2021).
6. Jin, X. *et al.* A metastasis map of human cancer cell lines. *Nature* **588**, 331–336 (2020).
7. Rogava, M. *et al.* Loss of Pip4k2c confers liver-metastatic organotropism through insulin-dependent PI3K-AKT pathway activation. *Nat. Cancer* **5**, 433–447 (2024).
8. Borgers, J. S. W. *et al.* Melanoma Metastases to the Adrenal Gland Are Highly Resistant to Immune Checkpoint Inhibitors. *J. Natl. Compr. Canc. Netw.* **19**, 53–63 (2021).
9. Tumeh, P. C. *et al.* Liver Metastasis and Treatment Outcome with Anti-PD-1 Monoclonal Antibody in Patients with Melanoma and NSCLC. *Cancer Immunol. Res.* **5**, 417–424 (2017).
10. Jee, J. *et al.* Automated real-world data integration improves cancer outcome prediction. *Nature* (2024) doi:10.1038/s41586-024-08167-5.
11. Nguyen, B. *et al.* Genomic characterization of metastatic patterns from prospective clinical sequencing of 25,000 patients. *Cell* **185**, 563-575.e11 (2022).
12. Kehl, K. L. *et al.* Assessment of Deep Natural Language Processing in Ascertaining Oncologic Outcomes From Radiology Reports. *JAMA Oncol.* **5**, 1421 (2019).
13. Kehl, K. L. *et al.* Artificial intelligence-aided clinical annotation of a large multi-cancer genomic dataset. *Nat. Commun.* **12**, 7304 (2021).
14. Lengel, H. B. *et al.* Genomic mapping of metastatic organotropism in lung adenocarcinoma. *Cancer Cell* **41**, 970-985.e3 (2023).
15. Patel, J. K., Didolkar, M. S., Pickren, J. W. & Moore, R. H. Metastatic pattern of malignant melanoma. *Am. J. Surg.* **135**, 807–810 (1978).
16. diSibio, G. & French, S. W. Metastatic Patterns of Cancers: Results From a Large Autopsy Study. *Arch. Pathol. Lab. Med.* **132**, 931–939 (2008).
17. Budczies, J. *et al.* The landscape of metastatic progression patterns across major human cancers. *Oncotarget* **6**, 570–583 (2015).
18. Riihimäki, M., Thomsen, H., Sundquist, K., Sundquist, J. & Hemminki, K. Clinical landscape of cancer metastases. *Cancer Med.* **7**, 5534–5542 (2018).

19. Garcia, E. P. *et al.* Validation of OncoPanel: A Targeted Next-Generation Sequencing Assay for the Detection of Somatic Variants in Cancer. *Arch. Pathol. Lab. Med.* **141**, 751–758 (2017).
20. Akbani, R. *et al.* Genomic Classification of Cutaneous Melanoma. *Cell* **161**, 1681–1696 (2015).
21. Sandru, A., Voinea, S., Panaitescu, E. & Blidaru, A. Survival rates of patients with metastatic malignant melanoma. *J. Med. Life* **7**, 572–576 (2014).
22. Sade-Feldman, M. *et al.* Resistance to checkpoint blockade therapy through inactivation of antigen presentation. *Nat. Commun.* **8**, 1136 (2017).
23. Bucheit, A. D. *et al.* Complete Loss of PTEN Protein Expression Correlates with Shorter Time to Brain Metastasis and Survival in Stage IIIB/C Melanoma Patients with *BRAF* V600 Mutations. *Clin. Cancer Res.* **20**, 5527–5536 (2014).
24. Robertson, A. G. *et al.* Integrative Analysis Identifies Four Molecular and Clinical Subsets in Uveal Melanoma. *Cancer Cell* **32**, 204-220.e15 (2017).
25. Assessment of Metastatic Disease Status at Death in 435 Patients With Large Choroidal Melanoma in the Collaborative Ocular Melanoma Study (COMS): COMS Report No. 15. *Arch. Ophthalmol.* **119**, 670 (2001).
26. Pérez-Guijarro, E. *et al.* Multimodel preclinical platform predicts clinical response of melanoma to immunotherapy. *Nat. Med.* **26**, 781–791 (2020).
27. Bald, T. *et al.* Ultraviolet-radiation-induced inflammation promotes angiotropism and metastasis in melanoma. *Nature* **507**, 109–113 (2014).
28. Day, C.-P. *et al.* 'Glowing head' mice: a genetic tool enabling reliable preclinical image-based evaluation of cancers in immunocompetent allografts. *PloS One* **9**, e109956 (2014).
29. Joosse, A. *et al.* Gender Differences in Melanoma Survival: Female Patients Have a Decreased Risk of Metastasis. *J. Invest. Dermatol.* **131**, 719–726 (2011).
30. Fane, M. E. *et al.* Stromal changes in the aged lung induce an emergence from melanoma dormancy. *Nature* **606**, 396–405 (2022).
31. Hodi, F. S. *et al.* Improved Survival with Ipilimumab in Patients with Metastatic Melanoma. *N. Engl. J. Med.* **363**, 711–723 (2010).
32. Wang, S., Riedstra, C. P., Zhang, Y., Anandh, S. & Dudley, A. C. PTEN-restoration abrogates brain colonisation and perivascular niche invasion by melanoma cells. *Br. J. Cancer* **130**, 555–567 (2024).
33. Zhao, J. *et al.* Immune and genomic correlates of response to anti-PD-1 immunotherapy in glioblastoma. *Nat. Med.* **25**, 462–469 (2019).
34. Peng, W. *et al.* Loss of PTEN Promotes Resistance to T Cell–Mediated Immunotherapy. *Cancer Discov.* **6**, 202–216 (2016).

35. Exposito, F. *et al.* PTEN Loss Confers Resistance to Anti–PD-1 Therapy in Non–Small Cell Lung Cancer by Increasing Tumor Infiltration of Regulatory T Cells. *Cancer Res.* **83**, 2513–2526 (2023).
36. Sade-Feldman, M. *et al.* Resistance to checkpoint blockade therapy through inactivation of antigen presentation. *Nat. Commun.* **8**, 1136 (2017).
37. Livingstone, E. *et al.* GNAQ and GNA11 mutant nonuveal melanoma: a subtype distinct from both cutaneous and uveal melanoma. *Br. J. Dermatol.* (2020).
38. Mengoni, M. *et al.* Transactivation of Met signaling by oncogenic Gnaq drives the evolution of melanoma in Hgf-Cdk4 mice. *Cancer Gene Ther.* (2024) doi:10.1038/s41417-024-00744-0.
39. Zhang, H. *et al.* Exosome-delivered EGFR regulates liver microenvironment to promote gastric cancer liver metastasis. *Nat. Commun.* **8**, 15016 (2017).
40. Küsters-Vandevelde, H. V. N. *et al.* Activating mutations of the GNAQ gene: a frequent event in primary melanocytic neoplasms of the central nervous system. *Acta Neuropathol. (Berl.)* **119**, 317–323 (2010).
41. Sheng, X. *et al.* GNAQ and GNA11 mutations occur in 9.5% of mucosal melanoma and are associated with poor prognosis. *Eur. J. Cancer* **65**, 156–163 (2016).
42. Martínez-Jiménez, F. *et al.* Pan-cancer whole-genome comparison of primary and metastatic solid tumours. *Nature* **618**, 333–341 (2023).
43. Alexandrov, L. B. *et al.* The repertoire of mutational signatures in human cancer. *Nature* **578**, 94–101 (2020).
44. Chakravarty, D. *et al.* OncoKB: A Precision Oncology Knowledge Base. *JCO Precis. Oncol.* 1–16 (2017) doi:10.1200/PO.17.00011.
45. Leisch, F. FlexMix: A General Framework for Finite Mixture Models and Latent Class Regression in *R. J. Stat. Softw.* **11**, (2004).
46. Birnbaum, B. *et al.* Model-assisted cohort selection with bias analysis for generating large-scale cohorts from the EHR for oncology research. Preprint at https://doi.org/10.48550/ARXIV.2001.09765 (2020).
47. Ma, X., Long, L., Moon, S., Adamson, B. J. S. & Baxi, S. S. Comparison of Population Characteristics in Real-World Clinical Oncology Databases in the US: Flatiron Health, SEER, and NPCR. Preprint at https://doi.org/10.1101/2020.03.16.20037143 (2020).
48. Cheng, D. T. *et al.* Memorial Sloan Kettering-Integrated Mutation Profiling of Actionable Cancer Targets (MSK-IMPACT). *J. Mol. Diagn.* **17**, 251–264 (2015).
49. Day, C.-P. *et al.* Lentivirus-mediated bifunctional cell labeling for in vivo melanoma study. *Pigment Cell Melanoma Res.* **22**, 283–295 (2009).
50. Michael, H. *et al.* Abstract 1037: Progression from melanocytic nevi to melanoma is

associated with increased genomic mutations in a UV-induced mouse model of human melanoma. *Cancer Res.* **77**, 1037–1037 (2017).

Figures

Figures for
"Clinico-genomic features predict distinct metastatic phenotypes in cutaneous melanoma"
Aprati et al.

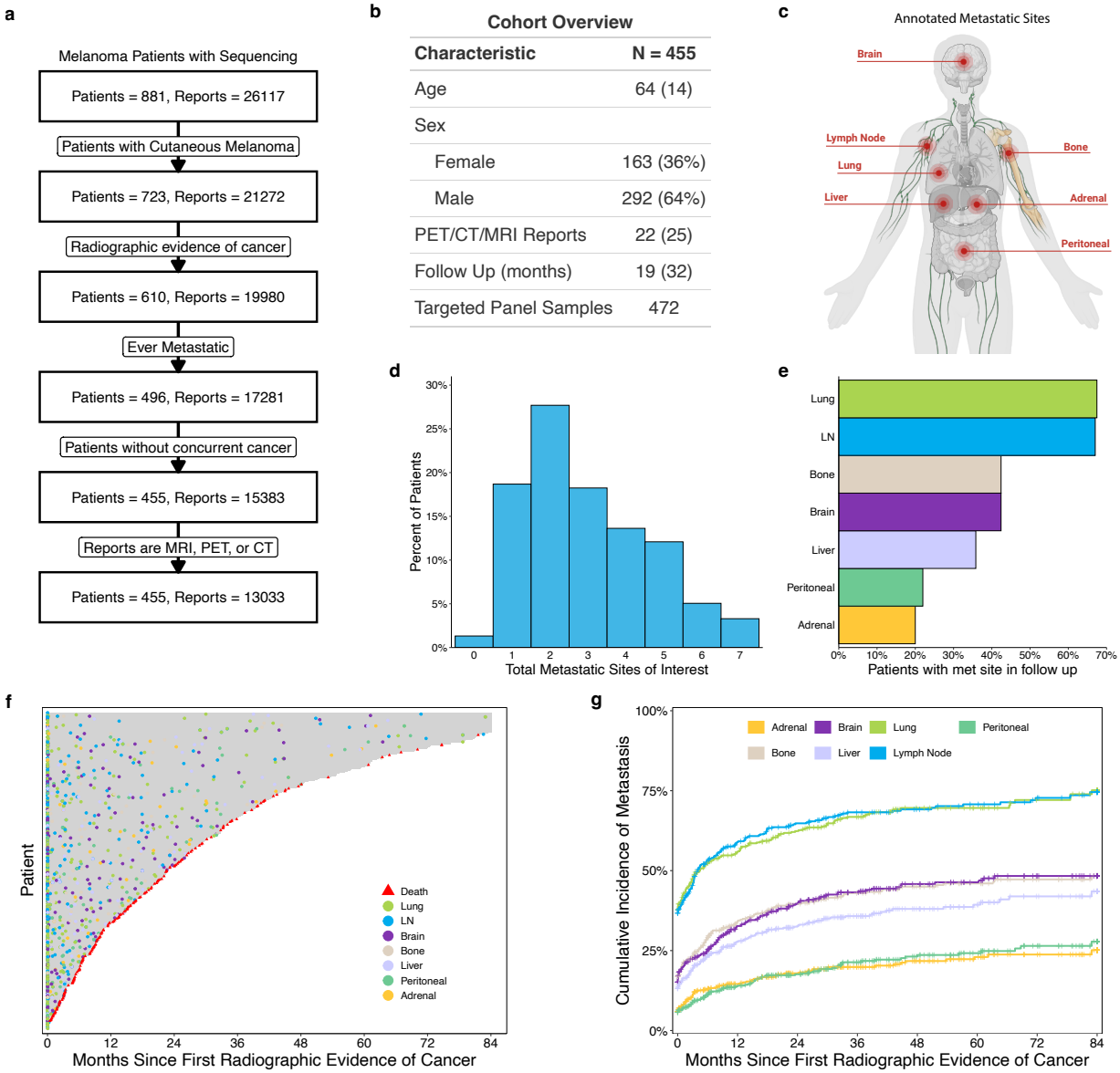

Figure 1. Cohort clinical characteristics and metastatic frequencies

a. Overview flowchart of imaging report filtering steps for cutaneous melanoma patients. **b.** Summary of cohort clinical characteristics. All statistics are presented as median (Standard deviation) or count. Follow-up time starts from date of first radiographic evidence of cancer. **c.** Schematic showing sites of metastasis annotated by the NLP model. **d.** Histogram of total distinct metastatic sites for all cutaneous patients in their lifetime. **e.** Overall frequency of metastatic sites for all cutaneous patients in the follow-up period. **f.** Event plots for cutaneous patients. Each row represents a patient, with metastatic events appearing as dots. Follow up for each patient ends with censoring or death. **g.** Cumulative incidence plot of each metastatic site for all cutaneous patients.

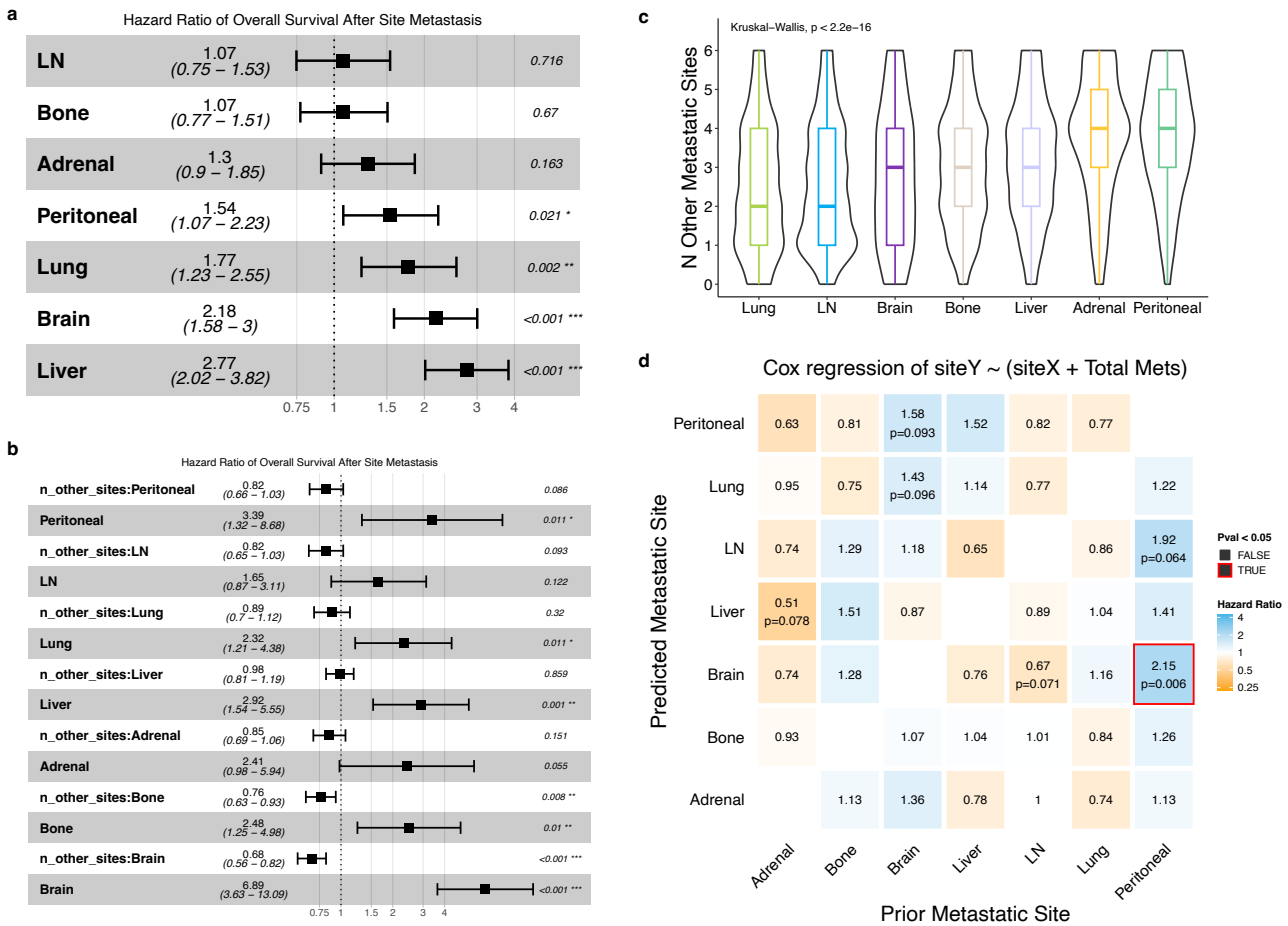

Figure 2. Associations of Site Metastasis on outcomes

a. Forest plot of multivariable cox regressions modeling the impact of each site on overall survival. Each site was run as an independent model of the form `OS ~ site + total other sites` with a term for the site of interest and a variable for total metastatic sites. Sites were encoded as time dependent covariates, and total sites was encoded as a cumulative time-dependent covariate. **b.** Forest plot of a multivariable cox regression showing the impact of each site and site interactions with total other metastatic sites on overall survival. Each site was run as an independent model of the form `OS ~ site * total other sites`. **c.** Violin and boxplots of total number of metastatic sites (lifetime) stratified by site. The area within each violinplot is normalized to be equivalent. **d.** Time dependent site-site associations. Squares represents the cox regression hazard ratio of the time dependent covariate prior metastatic site (X axis) with the incidence of the predicted metastatic site (Y axis). Total sites was included as a cumulative time dependent covariate in each model. Boxplots: Box limits indicate the IQR (25th to 75th percentiles), with the center line indicating the median. Whiskers show the values ranges up to 1.5 x IQR above the 75th or below the 25th percentiles. Forest plots: The center box indicates estimated HR with whiskers showing the range of the 95% confidence interval for the HR.

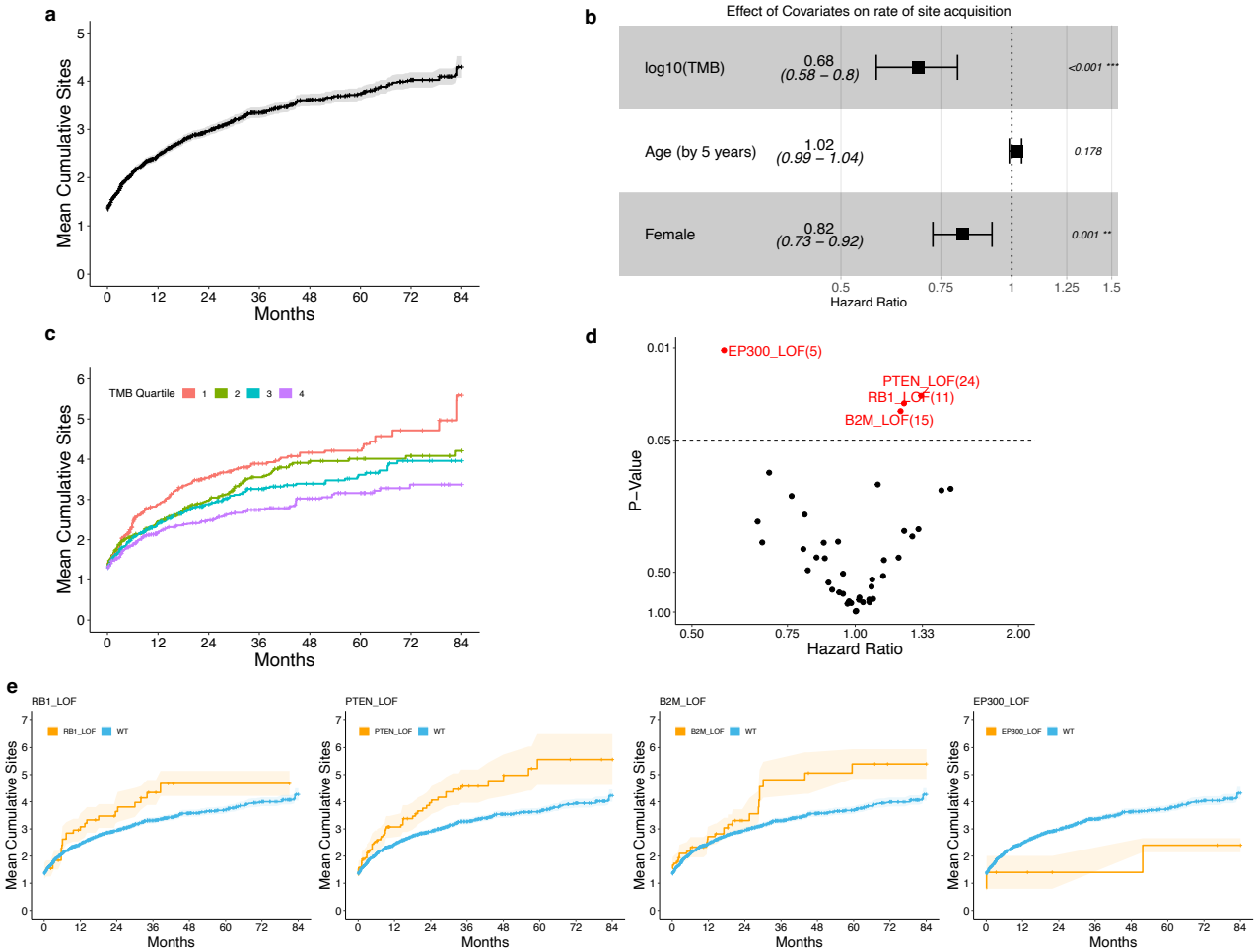

Figure 3. Correlates of Metastatic Potential

a. Estimated mean cumulative function of total distinct metastatic sites across patient follow-up. **b.** Estimated effect of clinical covariates on rate of new metastatic sites. The forest plot shows the results of a multivariable Andersen-Gill model for recurrent events. For forest plots, the center box indicates estimated HR with whiskers showing the range of the 95% confidence interval for the HR. **c.** Mean cumulative function of total distinct metastatic sites of patients stratified by TMB quartile. Quartile 1 represents the lowest TMB values. **d.** Volcano plot of univariable Andersen-Gill models for each gene. Genes where at least 5 patients were mutated are shown. **e.** Mean cumulative function of total distinct metastatic sites of patients stratified whether patients had functional mutations in select genes.

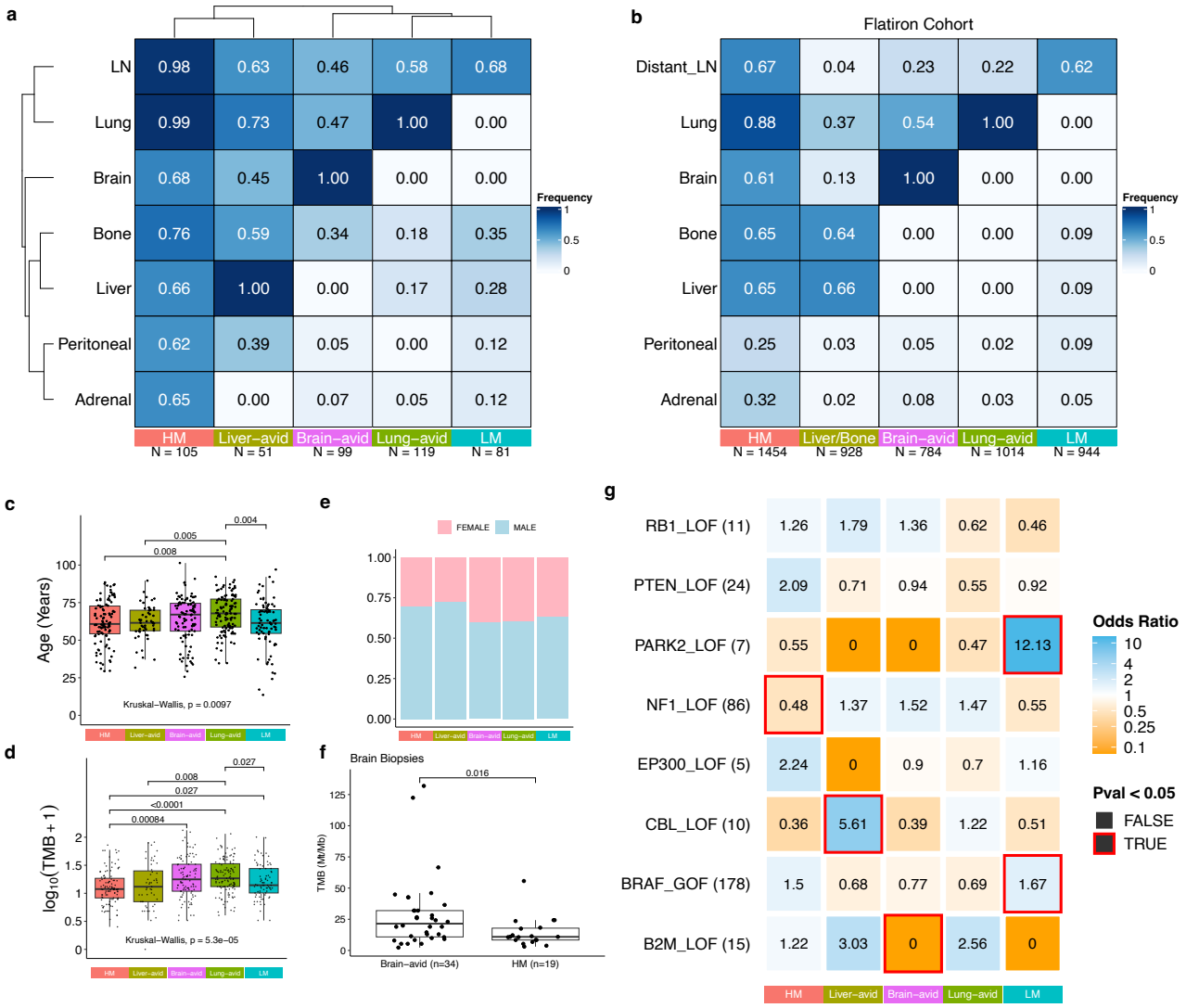

Figure 4. Patterns of metastasis across Cutaneous Melanoma Patients
a. Lifetime occurrence frequency of metastatic sites by cluster. Sites and clusters were grouped using hierarchical clustering. Numbers under each column are the total patients assigned to each cluster. **b.** Lifetime occurrence frequency of metastatic sites by cluster within the Flatiron cohort. Numbers under each column are the total patients assigned to each cluster. **c.** Boxplot of age at first radiographic evidence of cancer by cluster. **d.** Tumor mutational burden by cluster. Boxplots show $\log_{10}$TMB by cluster. **e.** Stacked barplot of sex proportions by cluster. **f.** Boxplot comparison for TMB values for brain biopsies from patients in the Brain-avid (n=34) or HM cluster (n=19). Test bar represents the p value of a wilcoxon rank sum test. **g.** Heatmap displaying enrichment of mutations by cluster. Each square represents a Fisher test of functional mutation occurrences in the specified cluster vs. all other clusters. Red borders represent tests with P-Values < 0.05. Numbers next to gene names refer to the number of patients with that functional mutation across the cohort. Boxplots: Box limits indicate the IQR (25th to 75th percentiles), with the center line indicating the median. Whiskers show the values ranges up to 1.5 x IQR above the 75th or below the 25th percentiles.

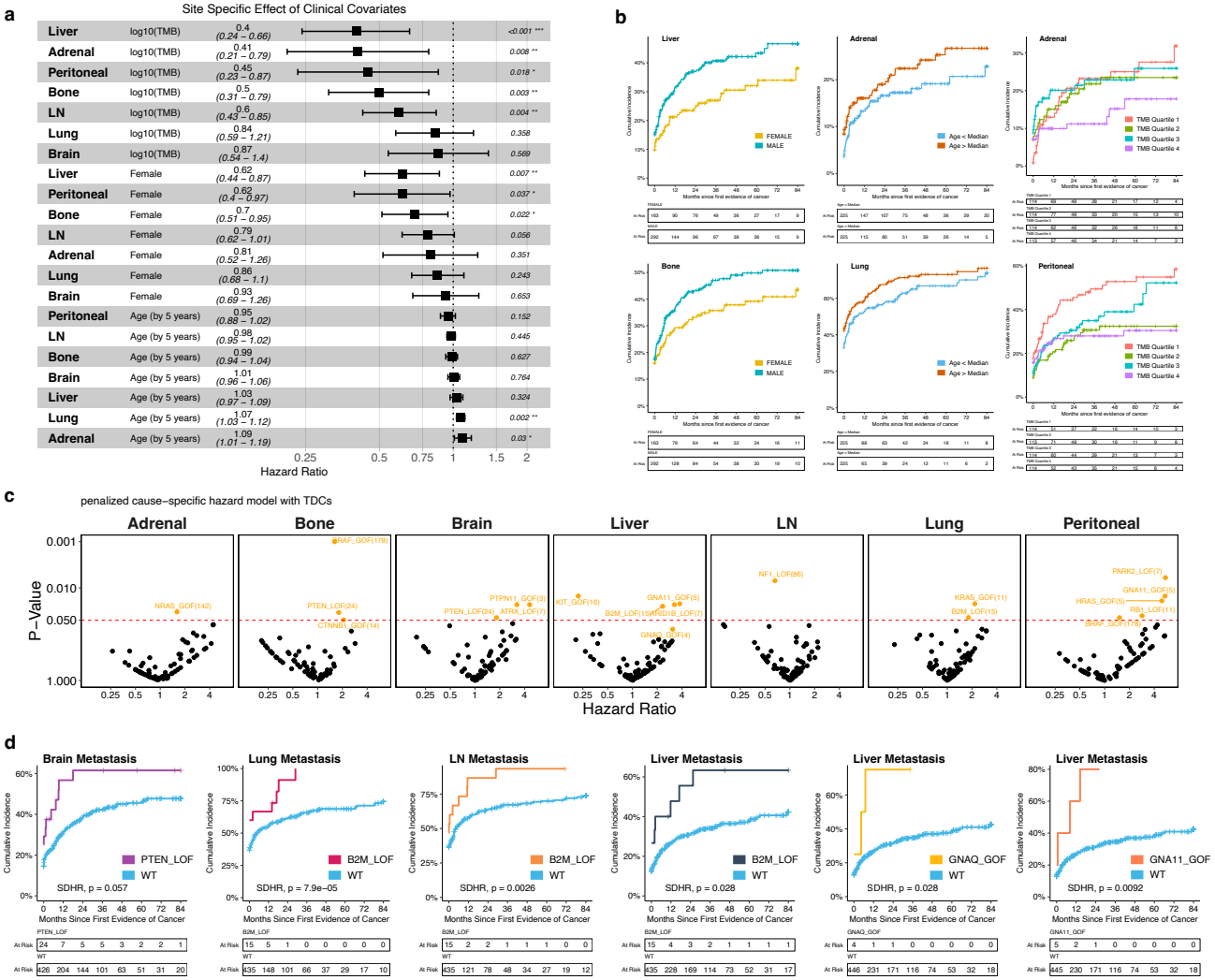

Figure 5. Associations of Site-Specific Metastasis

a. Forest plot displaying the results of multivariable cause-specific hazard models for clinical covariates. Models were distinct for each site, and included all covariates shown. Rows are sorted by covariate and then estimated hazard ratio. For forest plots, the center box indicates estimated HR with whiskers showing the range of the 95% confidence interval for the HR. **b.** Exemplary clinical covariate association site specific cumulative incidence curves. Cumulative incidence curves of liver metastasis stratified by sex, lung metastasis stratified by median split age, bone metastasis stratified by tumor mutational burden quartiles, and peritoneal metastasis stratified by tumor mutational burden quartiles. **c.** Associations of functional mutations in gene with site metastasis. Each box represents the model results for different metastatic sites. Each point represents the results from a penalized cause-specific hazard model with the incidence of the specific metastatic sites predicted by the functional mutation status of a gene. Total distinct metastatic sites was included in each model as a cumulative time dependent variable. Points colored orange are significant (Beta term P-Value < 0.05). **d** Select cumulative incidence curves highlighting site-specific associations. Patients are stratified by the functional status of the given gene. SDHR, p = subdistribution hazard ratio p-value.

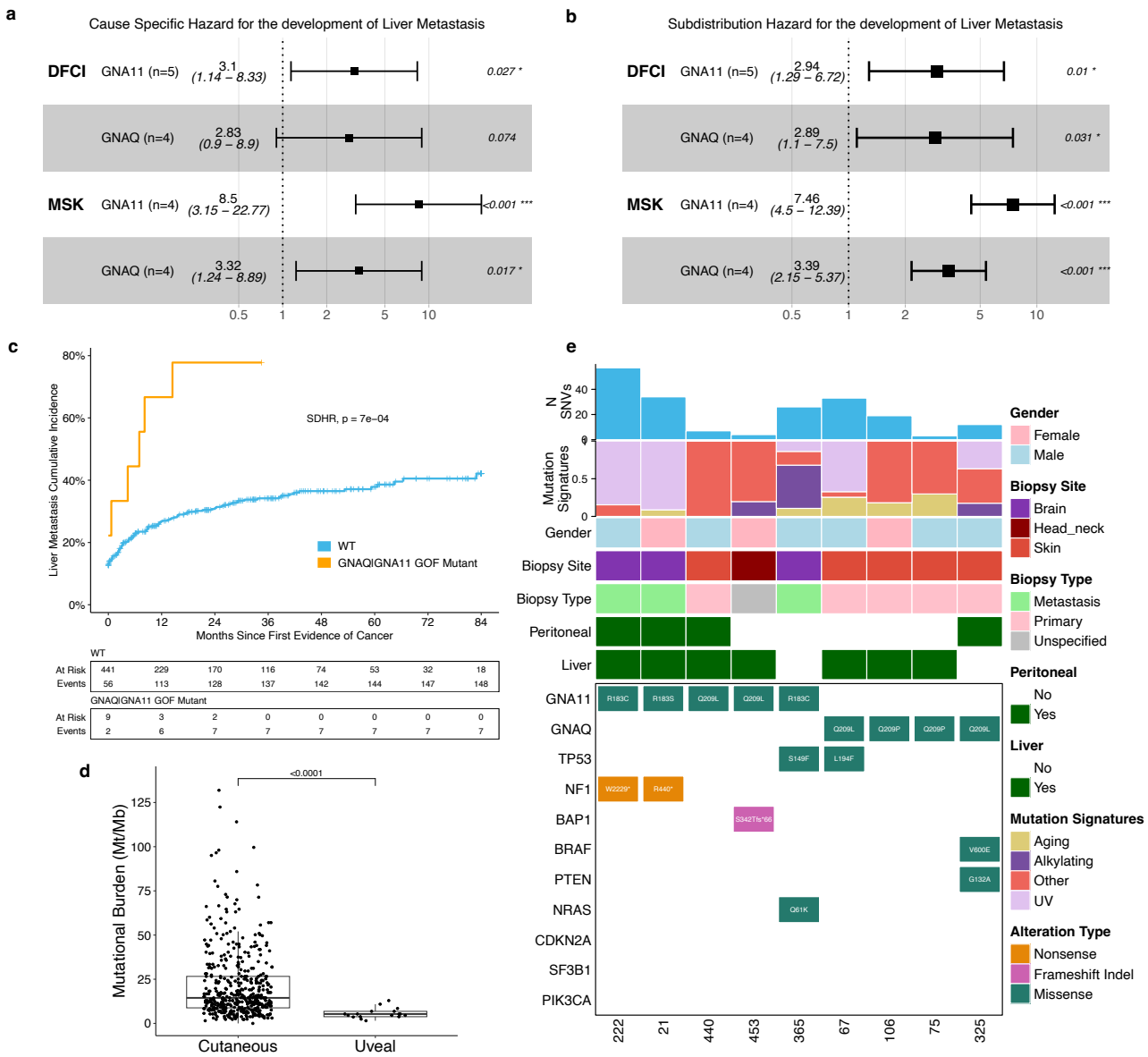

Figure 6. GNA11/GNAQ mutations confer liver metastasis in cutaneous melanoma patients **a-b.** Computational validation of the GNA associations. Forest plot of (a) cause-specific or (b) subdistribution hazard models for incidence of liver metastasis stratified by *GNA11* or *GNAQ*. The first two rows show the results in our cohort, and the last two rows show the results of the same analysis in the MSK cohort. For forest plots, the center box indicates estimated HR with whiskers showing the range of the 95% confidence interval for the HR. **c.** Cumulative incidence curve of liver metastasis stratified by whether cutaneous patients had gain-of-function mutation in either *GNAQ* or *GNA11*. **d.** TMB comparison of GNA patients with other cutaneous patients in the cohort and uveal melanoma patients (N=17). Test bars represent the p values from wilcoxon rank sum tests. **e.** Comutation plot showing select clinical and genomic characteristics for all cutaneous patients in the cohort with either a *GNA11* or *GNAQ* functional mutation (N=9 patients). Each column represents a patient and sequenced biopsy. Mutational signature refers to the inferred relative contribution of UV-induced mutations, alkylating DNA damage, Aging effect, or other mutational signatures. Liver status refers to whether the patient had a liver metastasis in the follow-up period. SF3B1 had no functional mutations across the patients. Boxplots: Box limits indicate the IQR (25th to 75th percentiles), with the center line indicating the median. Whiskers show the values ranges up to 1.5 x IQR above the 75th or below the 25th percentiles.

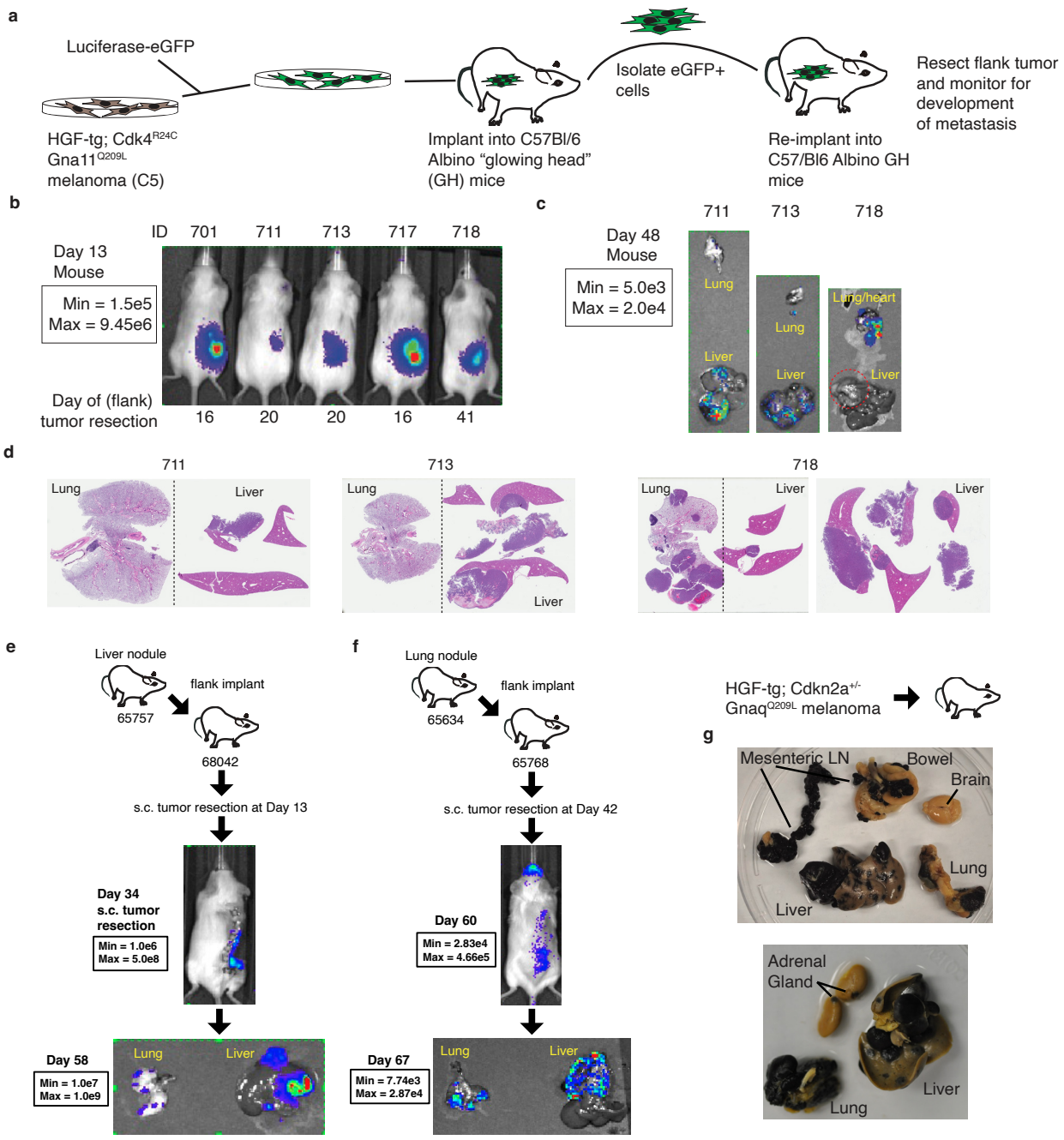

Figure 7. Liver metastasis in preclinical models of Gna11/Gnaq-mutated melanoma
a. Schematic of Gna11 melanoma model. Gna11-mutated HGF-tg;Cdk4^{R24C} melanoma line C5 was labeled with firefly (ff) luciferase/H2B-GFP genes ex vivo and then implanted into a syngeneic donor mouse. GFP+ cells were sorted from the harvested flank tumor or lung metastasis and then re-implanted into recipient albino C57Bl/6 GH mice. Primary flank tumors were resected and mice were monitored by bioluminescence imaging (BLI) for metastases. **b.** BLI of recipient mice on day 13 (n=5). Date below image represents day of primary tumor resection. **c.** BLI of harvested organs from recipients on day 48. **d.** Hematoxylin and eosin (H&E) staining of liver and lung from recipients on day 48. **e.** Exemplary experiment where liver metastases from a mouse with ff-Luc/GFP labeled GNA11 mutated tumors were re-implanted in the flank of recipient mice. Primary tumors were resected and mice monitored via BLI for metastases. BLI shown for mice on day 34. BLI of harvested organs from exemplary mouse at day 58 shown below. **f.** Exemplary experiment where lung metastases from a mouse with ff-Luc/GFP labeled GNA11 mutated tumors were re-implanted in the flank of recipient mice. Primary tumors were resected and mice monitored via BLI for metastases. BLI shown for mice on day 60. BLI of harvested organs from the mouse at day 67 shown below. **g,h.** Necropsy of organs harvested from two exemplary C57BL/6 mice implanted with HGf-tg;Cdkn2a$^{+/-}$ derived, Gnaq^{Q209L}-driven melanoma. Organs shown for mice include liver, lung, adrenal glands, brain, bowel, and mesenteric lymph nodes (LN).

Supplemental Information

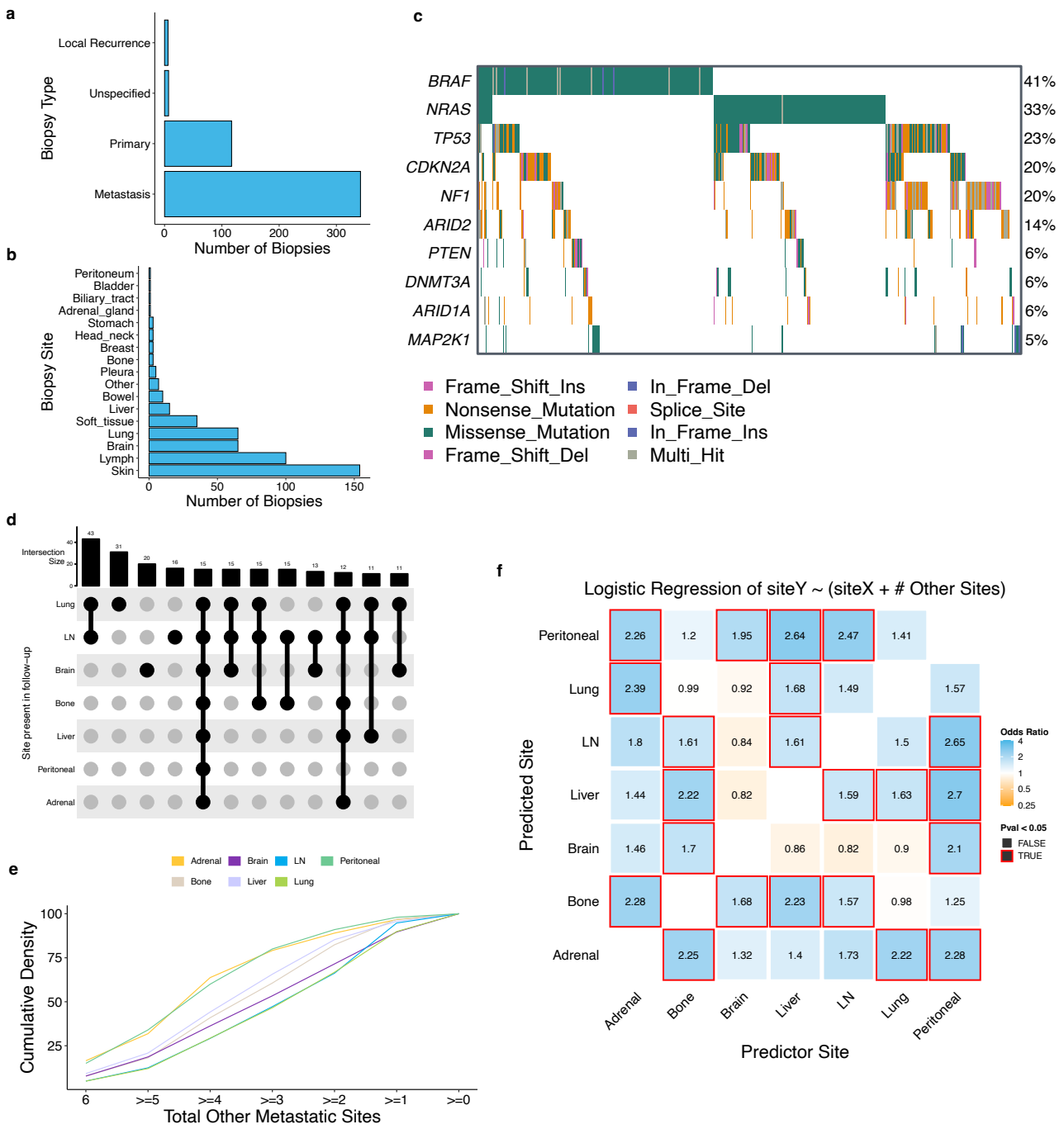

Supplementary Figure 1. Additional cohort overview and site metastasis outcomes
a. Distribution of biopsy types across the sequenced samples. **b.** Distribution of biopsy sites across the sequenced samples. **c.** Overview of the ten most frequent alterations in the cutaneous melanoma patients. Rows are genes, and columns represent individual patients. Total frequency of alterations across the cohort for each gene are labelled on the right side. BRAF, NRAS, and NF1 frequencies are similar to expected genomics of melanoma. **d.** Upset plot showing the frequency of lifetime metastatic patterns across the cohort. Patterns that occur in at least 10 patients are shown. **e.** Cumulative density curves of total other metastatic sites stratified by whether patients had that site in lifetime. **f.** Logistic regressions of site metastasis associations. Squares represents the logistic regression odds ratio of lifetime status of the predictor site (X axis) with the status of the predicted site (Y axis). A variable representing total other metastatic sites in lifetime (excluding the predictor and predicted sites) was included to control for overall site burden.

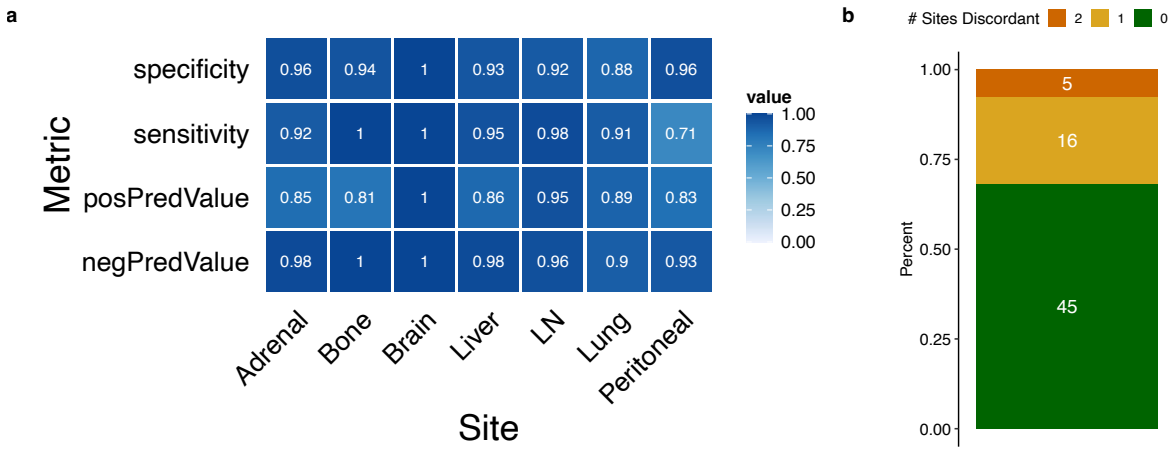

Supplementary Figure 2. NLP annotation performance compared to manual annotations
a. Performance metrics for NLP annotations compared to manual annotation ground truth for each metastatic site. **b.** Stacked barplot showing the number of discordant sites by patient between the NLP annotations and manual annotations. A low number of patients have multiple discordant site labels.

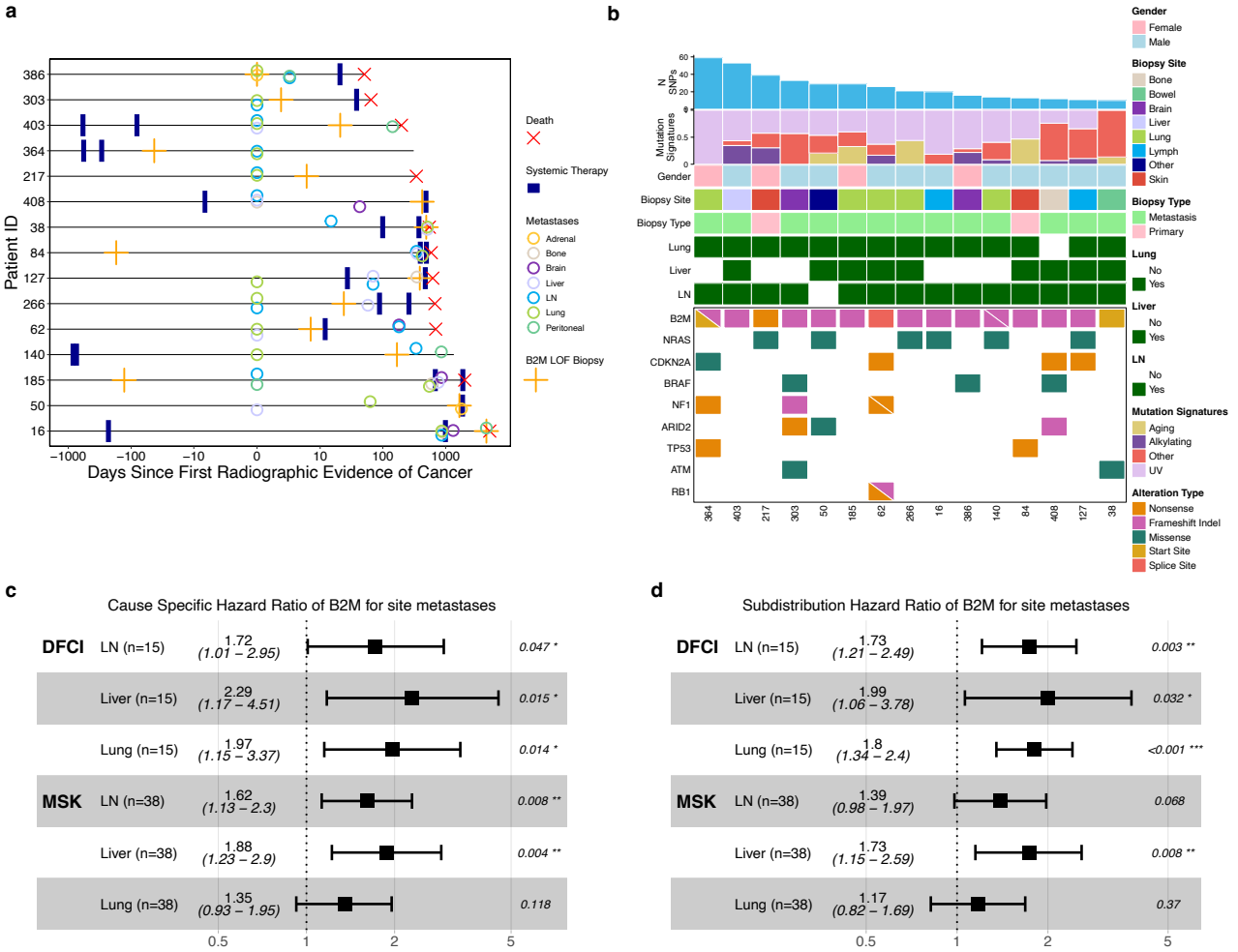

Supplementary Figure 3. B2M Exploration and Validation

a. Visualization of the patient history for *B2M* mutant patients. Grey bars represent the follow-up time for the patients based on imaging reports, starting at first radiographic evidence of cancer. Red Xs note death if occurred, and orange crosses mark the time at which the *B2M* mutated biopsy was taken. Colored dots represent time of first metastasis at a site, derived from our NLP annotations. Width of treatment bars correspond to length of treatment. Treatment that didn't have end date available were capped at 1 month after start time. **b.** Comutation plot showing clinical and genomic characteristics for all cutaneous patients in the cohort with *B2M* functional mutation (N=16 patients). Each column represents a patient and sequenced biopsy. Mutational signature refers to the inferred relative contribution of UV-induced mutations, alkylating DNA damage, Aging effect, or other mutational signatures. Liver, lung, LN status refers to whether the patient had that metastatic site in the follow-up period. **cd.** Computational validation of the B2M site metastasis associations. Forest plot of (c) cause-specific or (d) subdistribution hazard models for incidence of liver, lung, or LN metastasis stratified by *B2M*. The first three rows show the results in our cohort, and the last three rows show the results of the same analysis in the MSK cohort. For forest plots, the center box indicates estimated HR with whiskers showing the range of the 95% confidence interval for the HR.

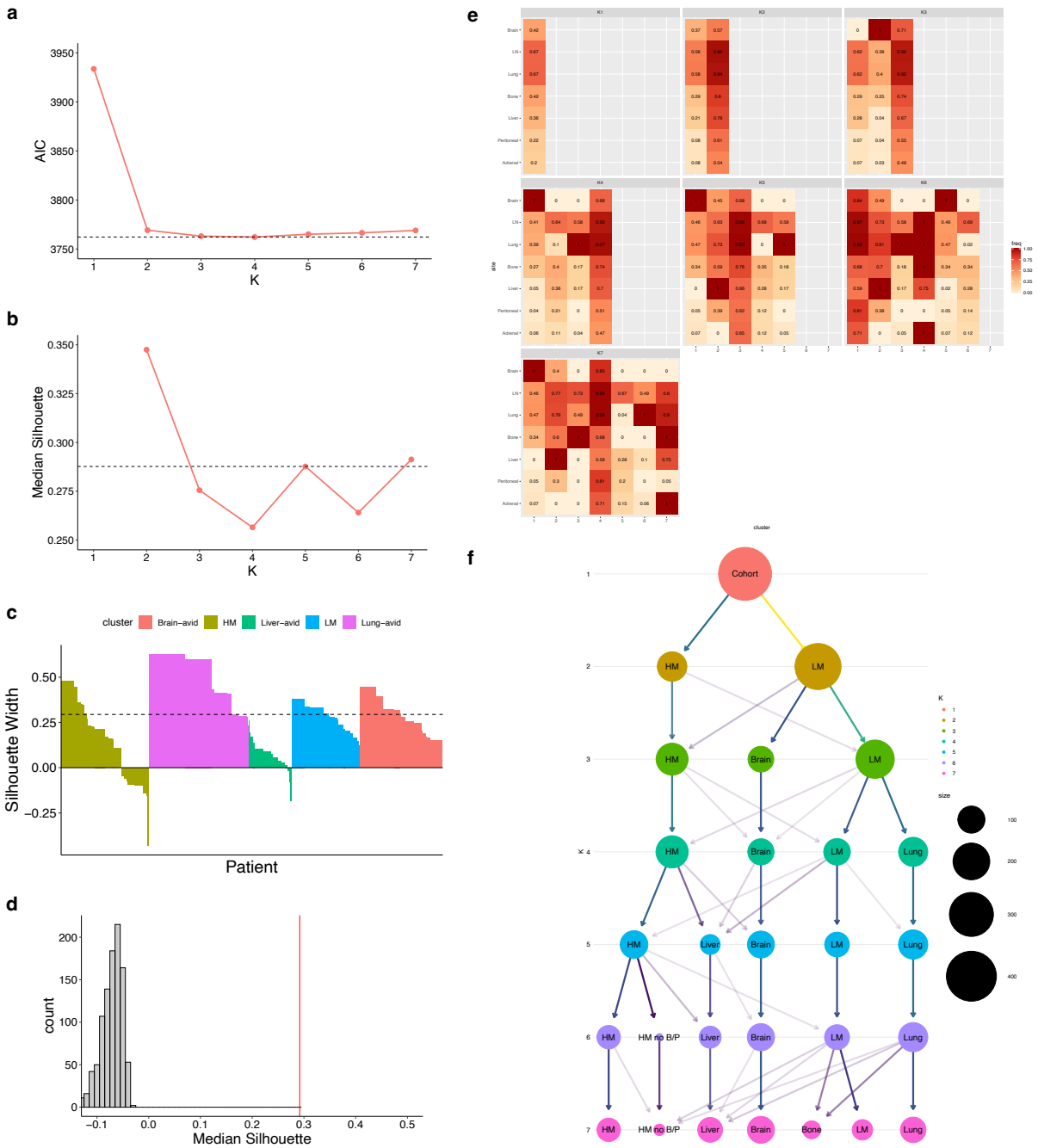

Supplementary Figure 4. Clustering metrics and cluster number selection
a. Plot of AIC metric for each value of k components for the Bernoulli mixture model. **b.** Median silhouette score for each value of k components for the Bernoulli mixture model. **c.** Plot of silhouette scores for each patient colored by cluster. Dashed line shows the average silhouette score across all patients. **d.** Heatmap of site frequency by cluster for each value of k components of the Bernoulli mixture model. **e.** Clustree visualization showing the size, interpretation, and movement of clusters as the value of k components changes in the Bernoulli mixture model. Darkness of arrows represent higher quantities of patients moving to a different cluster at different values of k components. Size of circles signify number of patients in the cluster. Color of circles signify value of k. HM = highly metastatic, LM = low metastasis, B/P = brain/peritoneal.

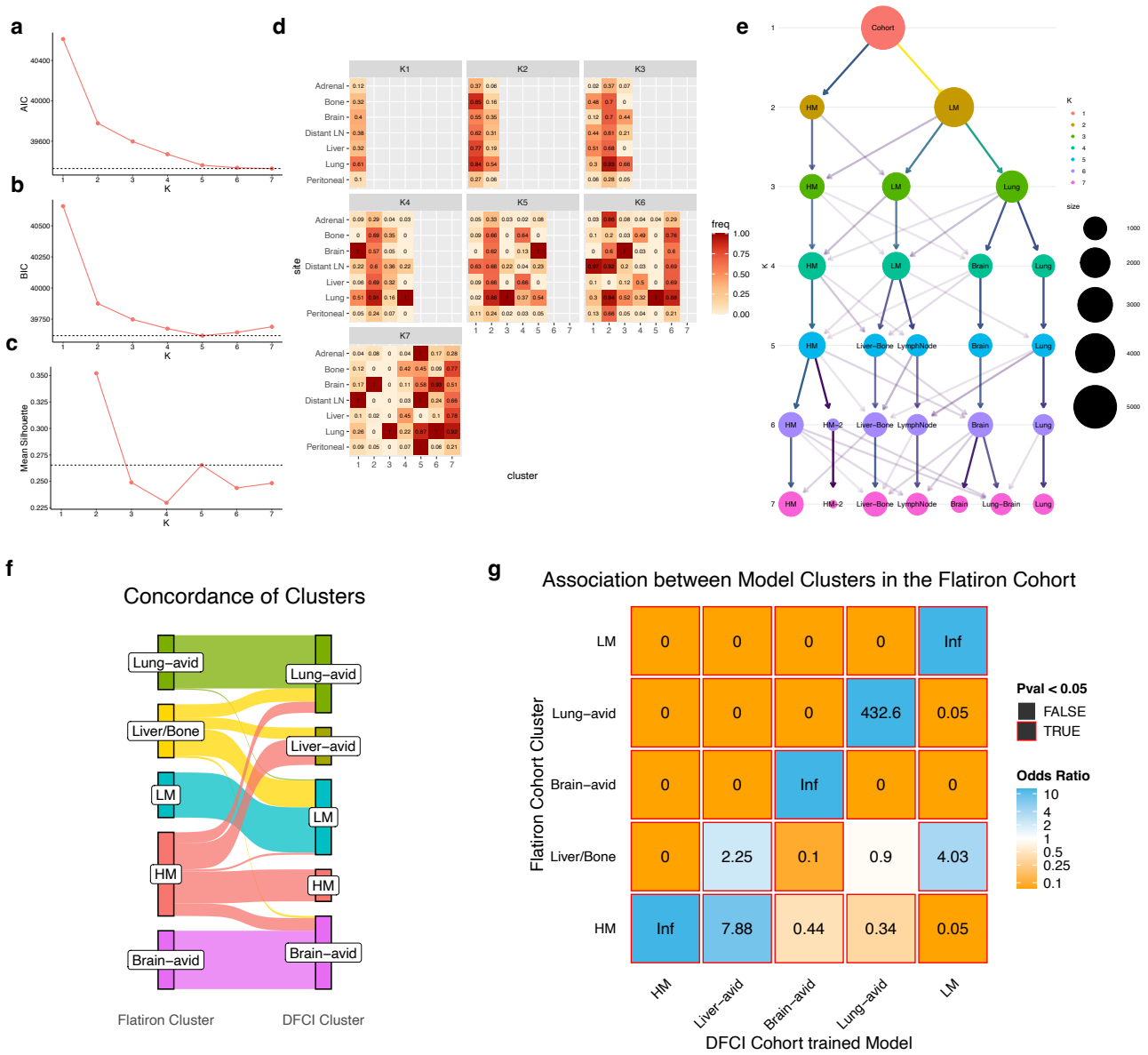

Supplementary Figure 5. Flatiron cohort cluster validation

a. Plot of AIC metric for each value of k components for the Bernoulli mixture model. **b.** Plot of BIC metric for each value of k components for the Bernoulli mixture model. **c.** Plot of mean silhouette score for each value of k components for the Bernoulli mixture model. **d.** Heatmap of site frequency by cluster for each value of k components of the Bernoulli mixture model. **e.** Clustree visualization showing the size, interpretation, and movement of clusters as the value of k components changes in the Bernoulli mixture model. Darkness of arrows represent higher quantities of patients moving to a different cluster at different values of k components. Size of circles signify number of patients in the cluster. Color of circles signify value of k. **f.** Sankey Diagram showing the clusters of the Flatiron cohort when called with the DFCI cohort trained model. **g.** Associations between clusters of Flatiron cohort patients called with model derived from either the Flatiron or DFCI cohort. Each square represents a Fisher exact test odds ratio of whether a patient is classified in a specific cluster with the DFCI trained model vs a specific cluster with the Flatiron trained model. Inf represents cases where all patients put into the cluster in one model were put into that same cluster in the other model or the case where none of the patients who were not in that cluster in one model are moved into that cluster in the other model. Red borders represent tests with P-value < 0.05.

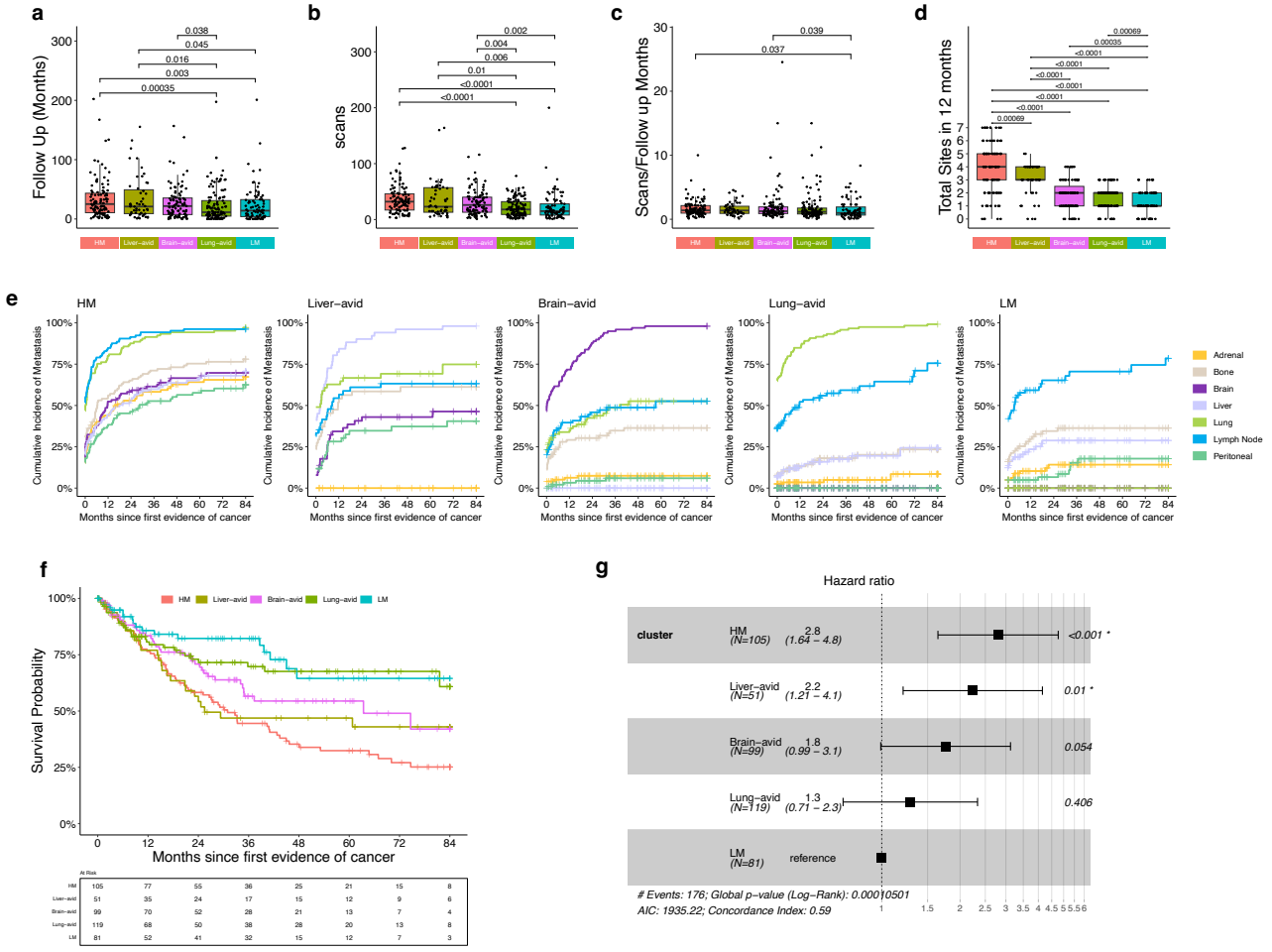

Supplementary Figure 6. Addition analysis of cluster covariates

a. Boxplots of follow up time by cluster. **b.** Boxplots of scan number by cluster. **c.** Boxplots of scans per month of follow-up by cluster. **d.** Boxplots of total metastatic sites within the first 24 months of follow-up by cluster. **e.** Cumulative incidence curves for each metastatic site stratified by cluster. **f.** Kaplan-Meier curves of overall survival stratified by cluster. **g.** Forest plot of cox proportional hazard model comparing survival by cluster. Reference group is the LM cluster. For forest plots, the center box indicates estimated HR with whiskers showing the range of the 95% confidence interval for the HR. Boxplots: Box limits indicate the IQR (25th to 75th percentiles), with the center line indicating the median. Whiskers show the values ranges up to 1.5 x IQR above the 75th or below the 25th percentiles. Comparison bars represent the results of wilcoxon tests. Only significant comparisons are shown.

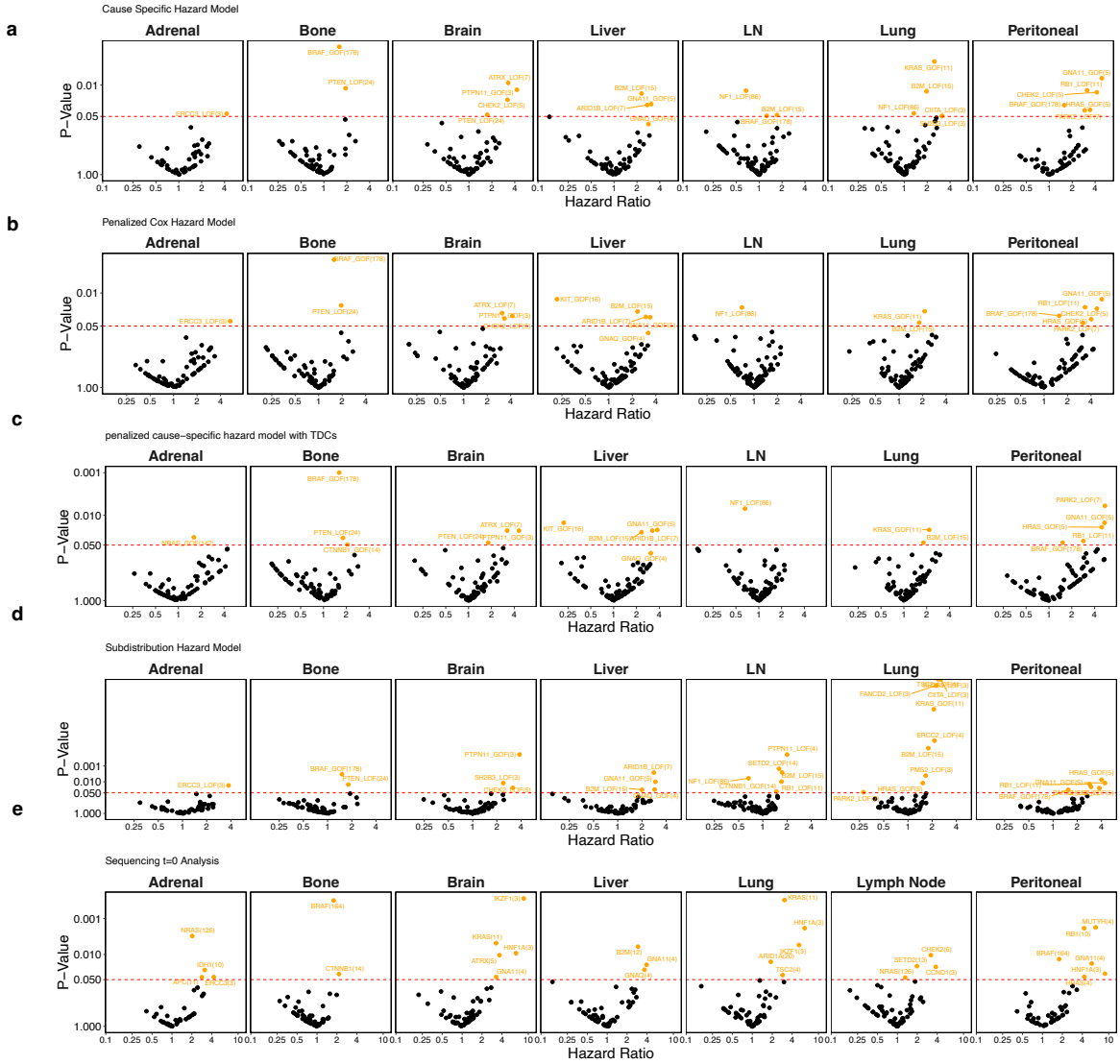

Supplementary Figure 7. Alternate Time to Metastasis Models

Associations of functional mutations in gene with site metastasis. Each box represents the model results for different metastatic sites. Each point represents the results of a model with the incidence of the specific metastatic sites predicted by the functional mutation status of a gene. Points colored are significant (Beta term p< 0.05) **a.** Volcano plots of cause-specific hazard model results. **b.** Volcano plots of subdistribution hazard model results. **c.** Volcano plots of penalized cause-specific hazard model results. **d.** Volcano plots of penalized cause-specific hazard model with total distinct metastatic sites was included as a cumulative time dependent variable. **e.** Volcano plots of sequencing time 0 based data with cause-specific hazard model results.

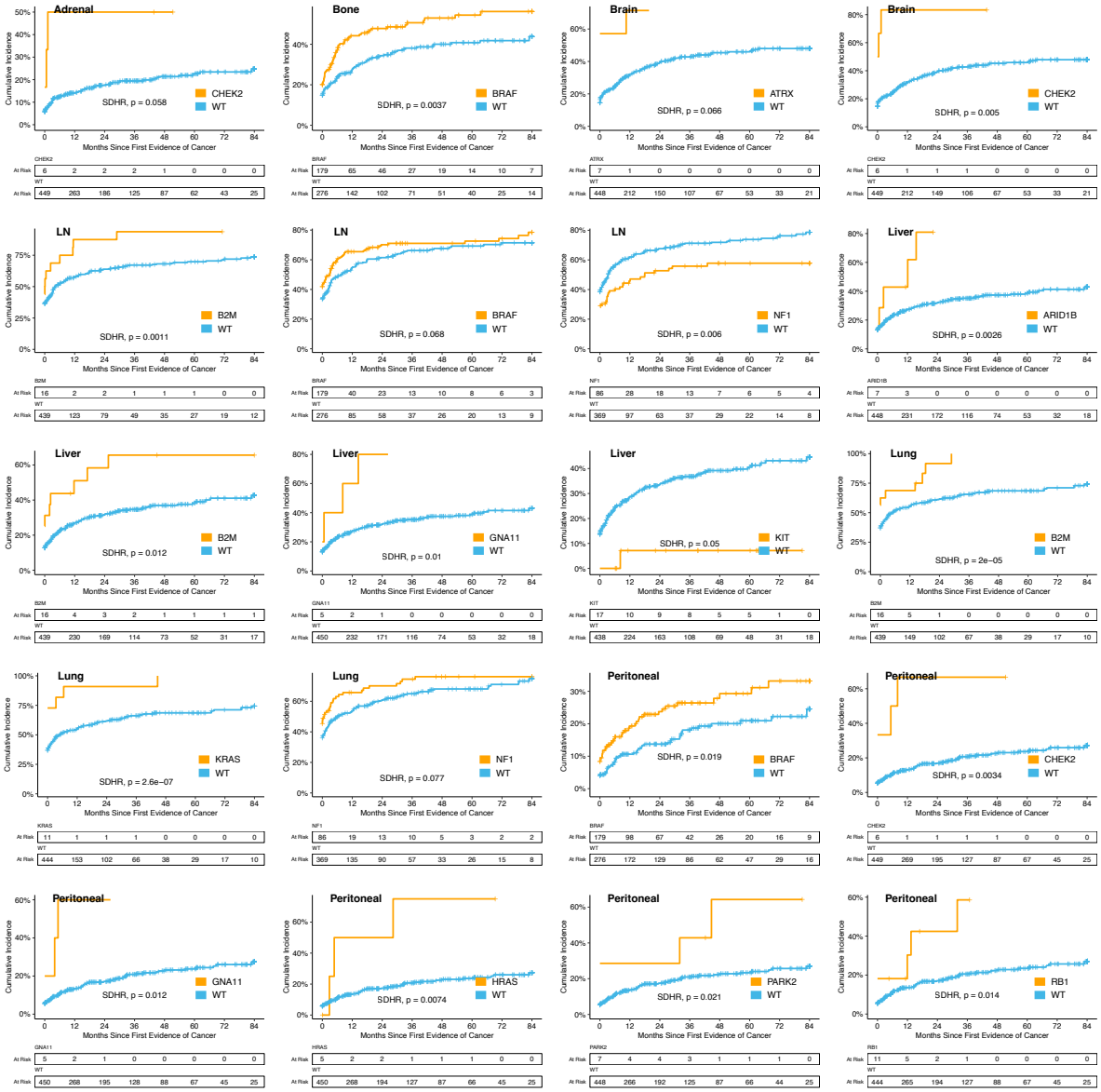

Supplementary Figure 8. Additional significant CIFs of site-specific metastasis
Cumulative incidence curves of metastasis for specific sites stratified by functional mutations in specific genes. SDHR = subdistribution hazard ratio, p = nominal p-value of subdistribution beta term for gene mutations.

a

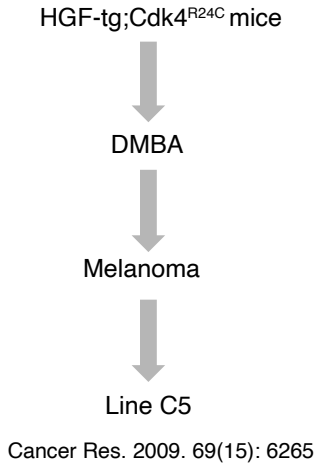

b

Gene	Mutation	VAF
Cdk4	R24X	0.98
Ercc4	I760F	0.38
Gna11	Q209L	0.4
Grin2a	R76H	0.38
Grin2b	Q105L	0.47
Map2k4	R132W	0.98
Mitf	C306fs	0.49
Trp53	R172H	1.0

c

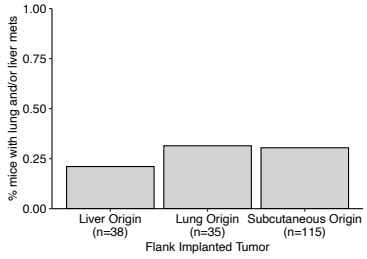

d

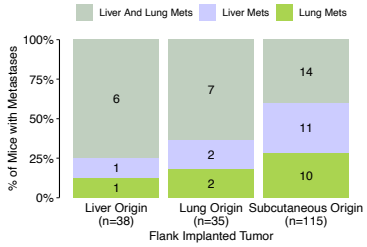

Supplementary Figure 9. Mouse model generation and further experiment results
a. Schematic for the generation of the C5 melanoma cell line. **b.** Results of genomic sequencing of the C5 melanoma cell line. **c,d.** Results from repeating the experiment shown in Figure 7d-e. **c.** Bar plots showing the percentage of mice that developed liver and/or lung metastases after being implanted with tumors originating from different sites. **d.** Stacked bar plots showing the proportions of mice that developed either liver metastases only, lung metastases only, or both lung and liver metastases. Annotation of n refers to the total mice implanted with tumors from the respective origin site.